Development, tests and calibration of electronic modules for measuring and monitoring the gas pressure in CMS muon chambers

von
Pim Rütten

Diplomarbeit in Physik

vorgelegt der

Fakultät für Mathematik, Informatik und Naturwissenschaften

der RWTH Aachen

im April 2005

angefertigt im
III. Physikalischen Institut A

Prof. Dr. Th. Hebbeker
(Erstgutachter)

Prof. Dr. M. Tonutti
(Zweitgutachter)

Contents

1. Introduction

From the very beginning mankind has been investigating its environment and a huge number of theories have been developed to describe it. From the Greek philosophers until now a lot has been learned about what the world is made of. We have come from the elements of fire, water, air and soil to the Standard Model of elementary particle physics which is the based upon the theory of relativity and quantum mechanics. It describes the forces of nature with 12 elementary particles (6 quarks and 6 leptons) and 3 interactions between them (strong, electromagnetic and weak force). Now it is up to the experimenters to confirm the theory's predictions or to prove it wrong. And this has been done in all modern particle accelerators. Up to now, no exception from the SM has been found, but we know that, although the SM does not have to be "wrong", there has to be more.

Still we have some unanswered questions. We don't know how matter gets its mass or if the quarks and leptons really are elementary particles or how one of the known forces, gravity, fits in with the others. To try and find the answers to these questions and to test extended versions of the standard model and other theories, a new high-energy particle collider, LHC, is being built at the European laboratory CERN in Geneva, Switzerland. The four main experiments that will conduct these and other tests are ALICE, ATLAS, CMS and LHC-B.

The *III. Physikalisches Institut A* of the RWTH Aachen is involved in one of these experiments; in CMS. For this experiment it manufactures drift chambers (muon chambers) for the muon system. One such chamber is composed of 3 so-called Super Layers, which in turn are made of 4 layers of several gas-filled drift cells. The functionality of such a drift cell depends, among other things, on the mixture and pressure of the gas that is used. Therefore the pressure is monitored with a system including pressure sensors and a read-out board that digitizes the data from the sensors.

The tests that were conducted with a number of versions of this read-out board and the calibration of the final version is the main subject of this diploma thesis.

2. Search for new particles

This chapter will give a short description of our current understanding of what the world is made of and what is holding it together. The theories that are desribed predict the existence of particles that have not been found yet. International collaborations are making an effort to find these missing particles.

2.1. What are we looking for?

2.1.1. The standard model

Throughout history physicists have tried to identify the fundamental building blocks that can describe everything around us. With increasing knowledge, which particles are considered fundamental has changed with time.

Modern theory, the standard model, tries to explain phenomena with the properties and interactions of a small number of three different kinds of particles that are considered fundamental, which means they have no internal structure and no excited states. These are leptons and quarks (spin-$\frac{1}{2}$ fermions) as the building blocks and spin-1 bosons as the "force carriers".

There are 4 fundamental forces of nature known today: the electromagnetic interaction (e^- bound in atoms), the weak interaction (β-decay), the strong interaction (quarks bound in hadrons) and gravity. The last one, gravity, is neglected in the standard model because it is very small compared to the other three.

The spin-1 bosons associated with the first three forces are respectively: the photon, the W- and Z-boson and the gluon. Since the range of an interaction scales with $1/M_{Boson}$, the electromagnetic interaction is long range ($M_{photon} = 0$), the weak interaction is short range (the two bosons are very heavy). The strong interaction is long range in principle ($M_{gluon} = 0$) but gluons cannot exist as free particles (like photons). They are bound by a potential $V \sim r$ ($r \geq 1$ fm) due to their "color" charge. The strong interaction therefore has a short range.

Leptons are spin-$\frac{1}{2}$ fermions without strong interaction. There are 6 known leptons (electron, muon, tauon and the corresponding neutrinos ν_e, ν_μ, ν_τ) occurring in so-called "generations" that are written in doublets. Each generation has a conserved quantum number associated with it.

$$\begin{pmatrix}\nu_e\\ e^-\end{pmatrix} \quad , \quad \begin{pmatrix}\nu_\mu\\ \mu^-\end{pmatrix} \quad , \quad \begin{pmatrix}\nu_\tau\\ \tau^-\end{pmatrix}.$$

The charged leptons (e^-, μ^-, τ^-) interact via electromagnetic and weak force, the neutral neutrinos via weak force only. In addition there is an antiparticle for each lepton, which makes a total of 12.

Quarks are spin-$\frac{1}{2}$ fermions that interact strongly. In analogy to the leptons, there are 6 known quarks (quark "flavours": up, down, charm, strange, top and bottom) occurring in 3 generations

$$\begin{pmatrix} u \\ d \end{pmatrix} \quad , \quad \begin{pmatrix} c \\ s \end{pmatrix} \quad , \quad \begin{pmatrix} t \\ b \end{pmatrix}.$$

and their corresponding anti quarks. The upper quark of each generation has charge $+\frac{2}{3}$, the lower quark has charge $-\frac{1}{3}$. The definition of their masses is difficult. Used are effective masses, obtained from high-energy scattering processes.

The standard model is a quantum field theory, based upon the $SU(3)_C \otimes SU(2)_L \otimes U(1)_Y$-symmetry group. Strong interaction is described by $SU(3)_C$, electroweak interaction by $SU(2)_L \otimes U(1)_Y$ and electromagnetic interaction by $U(1)_{EM}$, which is a subgroup of $SU(2)_L \otimes U(1)_Y$.

QED[1], represented by the $U(1)_{EM}$-symmetry group, is an example of a gauge theory. This means that it is invariant under gauge transformations of the 4-potential when the phase of the wave function of charged particles is transformed simultaneously. This argumentation can be reversed and then leads to the "gauge principle". This implies that the Dirac-equation is not gauge invariant, unless there is an external field with a coupling to charged particles. The quanta of such a field, gauge bosons, have to have zero mass, because gauge invariance is only valid for massless vector fields.

This is no problem in QED, since the gauge bosons, the photons, are massless. Also in the strong interaction this principle could be applied, but a problem seems to arise in weak interactions, where the gauge bosons W and Z are very heavy. This is were the Higgs field comes into play. It shields the long range of the weak interaction, which can in principle be described by a gauge invariant theory and thus has infinite range. The shielding (interaction) then gives the gauge bosons their masses, although the original gauge invariance still exists as a "hidden", also referred to as "spontaneously broken", gauge invariance.

Because three massive gauge bosons are needed, the following approach with four real Higgs fields is chosen:

$$\Phi \;=\; \begin{pmatrix} \phi^+ \\ \phi^0 \end{pmatrix} \;=\; \frac{1}{\sqrt{2}} \begin{pmatrix} \phi_1 + i\phi_2 \\ \phi_3 + i\phi_4 \end{pmatrix}. \tag{2.1}$$

They have a non-linear potential of the form

$$V(\phi) \;=\; -\mu^2 \Phi^\dagger \Phi + \lambda^2 (\Phi^\dagger \Phi)^2, \qquad v \equiv \frac{\mu}{\lambda} \tag{2.2}$$

which is added to the Lagrangian density $\mathcal{L}$ for massless charged particles:

[1] **Q**uantum **E**lectro**d**ynamics

$$\mathcal{L} = (D_\mu\phi)(D^\mu\phi)^* - V(\phi) - \frac{1}{4}F_{\mu\nu}F^{\mu\nu}. \tag{2.3}$$

Here $(D_\mu\phi)(D^\mu\phi)^*$ describes the coupling to the electromagnetic field A_μ with the covariant derivative $D_\mu = \delta_\mu + ieA_\mu$ and $F^{\mu\nu}$ represents the kinetic term for free massless Photons.
The ground state of ϕ, where V is minimal, will not be 0 (Figure 2.1), but rather

$$\phi_0 = \frac{\mu}{\sqrt{2}\lambda}e^{i\theta}, \qquad \theta = \arctan\frac{\phi_2}{\phi_1}. \tag{2.4}$$

In priciple, θ is arbitrary because of the rotational symmetry of the potential. The choice of $\theta = 0, \Phi = \binom{0}{v/\sqrt{2}}$ breaks this symmetry and results in masses for the gauge fields W^+, W^- and Z, while the photon γ remains massless. This is known as the "Higgs mechanism" [?].

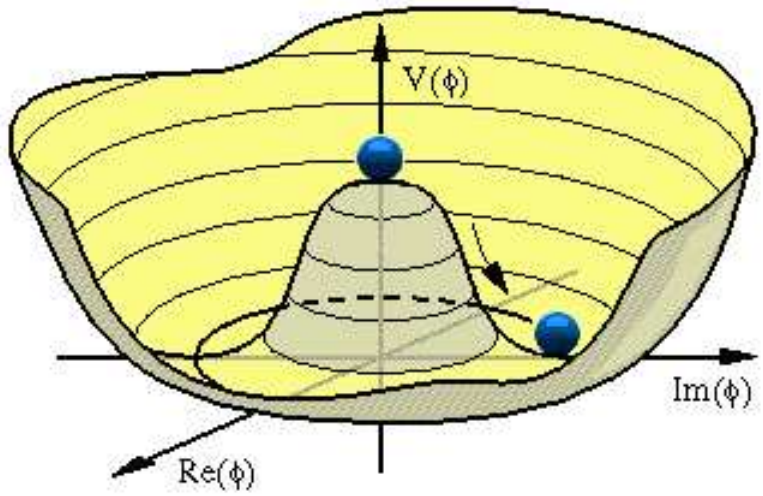

Figure 2.1.: The Higgs potential. As soon as θ is chosen, the symmetry is broken [?].

In breaking the symmetry, three of the four degrees of freedom (scalar fields in Φ) are used to give the three vector bosons their masses. One scalar field, the Higgs field, remains and can be identified with a particle, the Higgs boson H^0, which is the last particle in the standard model that has not been found yet.

The next step in the search for the Higgs boson will be a new particle accelerator, the LHC (section 3.1), that is under construction at CERN in Geneva. How the H^0 can be produced and detected with this facility, is described in 2.3 and 2.4.

2.1.2. Beyond the standard model

Despite the success of the standard model there are many questions unanswered. Physics at higher energies cannot be described by the standard model, there is no con-

nection between fermions and bosons, there are no serious candidates for dark matter and gravity is not incorporated.

To solve (a number of) these problems, theories have been developed that expand the standard model, incorporating it as a low-energy limit.

- Grand Unified Theories (GUTs)

  Their goal is to unite strong and electroweak interactions by describing them by a single coupling constant at an energy scale of about 10^{15} GeV. The differences between the coupling constants emerge when interpolating downwards to currently available energies.

- Supersymmetry (SUSY)

  In a SUSY-model it is assumed that every known elementary particle has a supersymmetrical partner, that has exactly the same properties, except for the spin, which differs by 1/2. A new multiplicative quantum number is needed. This "R-parity", $R = +1$ for "normal" particles and $R = -1$ for their superpartners, is a conserved quantity for reactions in the Minimal Supersymmetrical extension of the Standard Model (MSSM). This model uses the minimum number of couplings that are needed to produce the observed quantities of particles. Like the standard model it also contains Higgs fields.
  This symmetry, however, cannot be exact, because in this case most of the SUSY-particles would have already been found.

- String theories

  In string theory the point-like elementary particles are replaced by quantized one-dimensional strings that oscillate in N-dimensional space. This makes it possible to incorporate all interactions, including quantum gravity.

2.2. Luminosity and cross section

In this section a few physical quantities, common to elementary particle physics and accelerators, are described that will be used later.

Modern accelerators do not accelerate single particles, but "bunches" of particles. For bunches that fly in opposite directions with a circular frequency f, the event rate at an interaction point is given by
[?]

$$\frac{\mathrm{d}N}{\mathrm{d}t} = \frac{\sigma}{A} \cdot f = L\sigma, \tag{2.5}$$

where A is the area perpendicular to the beam axis in which the particles are likely to be found and the cross section σ is the effective area of the target (in this case the particles coming from the opposite direction). With a number of bunches n_B and n partcles per bunch, this yields for the luminosity L:

$$L = \frac{n_B \cdot f \cdot n^2}{A} \tag{2.6}$$

with $A = 4\pi\sigma_x\sigma_y$ and σ_x, σ_y the Gaussian distributions of the bunches in the directions perpendicular to the beam axis[?].

2.3. Higgs-production in the standard model

There are four main production channels for the standard model Higgs boson at the LHC-collider (section 3.1). Figure 2.2 shows the cross sections of these channels.

- Gluon-gluon-fusion.
  Although gluons do not couple directly to the Higgs boson, because they are massless, it is the dominant production process for H^0. Gluons couple to quarks via their color. The quarks then couple to the Higgs boson. Because this coupling is proportional to the fermion mass m_f, the coupling to gluons will be through virtual top quark loops.

- Vectorboson fusion.
  Two quarks emit two gauge bosons which then form a H^0 in the final state. The emission of a Z^0 does not affect the quark flavor, where the emission of a $W^{\pm}$ changes the flavor.

- Higgs radiation.
  A pair of quark-antiquark forms a virtual W^* or Z^* which then emits a Higgs boson.

- Associative production with top-antitop-pairs.
  This process is interesting because the final state with two top quarks and a Higgs boson makes it clearly separable from others.

2.4. Decay of the Higgs boson

Because it does not interact except through its mass, the Higgs boson can only be detected via its decay products. Higgs-decays can be divided into two classes, depending on the decay products: decays with massive products and decays with massless products. The Higgs boson couples directly to massive particles, which means there is also a direct decay process. Massless particles couple indirectly and therefore these decays need processes with loops of massive particles.

Free gluons and quarks that are produced in the decays cannot exist because of their color charge. They therefore form hadrons as a final state, which is called "fragmentation". This then leads to so-called "jets" of particles.

Figure 2.3 shows the branching ratio for the decay processes. As with the Higgs-production, the coupling is proportional to the mass of the particle. This means that the Higgs boson primarily decays into heavy particles. For high Higgs-masses $t\bar{t}$ final state decreases with respect to W^+W^- and Z^0Z^0 decreases because the coupling of both bosons is proportional to the cubic Higgs-mass while the coupling of the top quark is only linearly dependent on m_H. An interesting decay channel is the one where the final

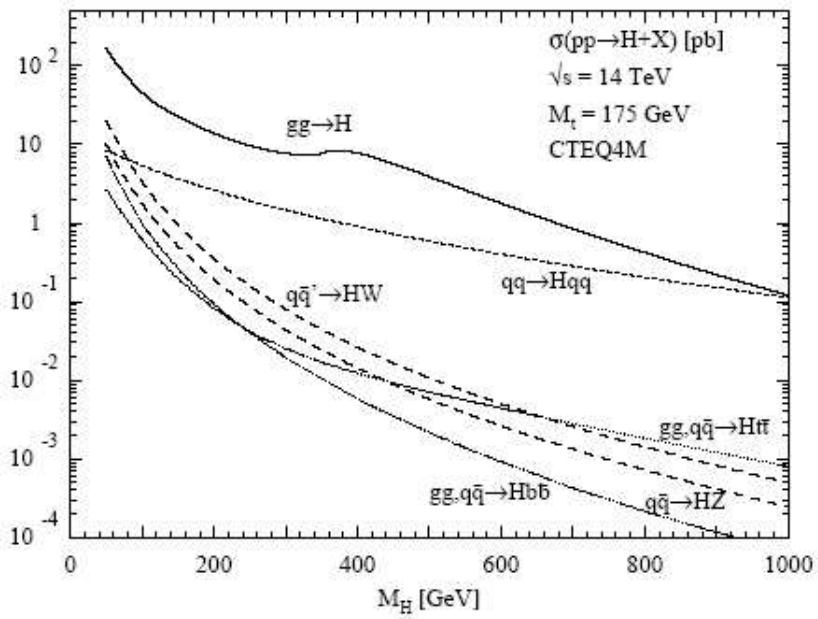

Figure 2.2.: Cross sections [pb] of several production processes of the Higgs boson, shown for Higgs masses from 0 to 1000 GeV. The dominant process by far is gluon-gluon-fusion [?].

state has 4 muons. These will have a distinct signature in the CMS detector, especially in the muon stations.

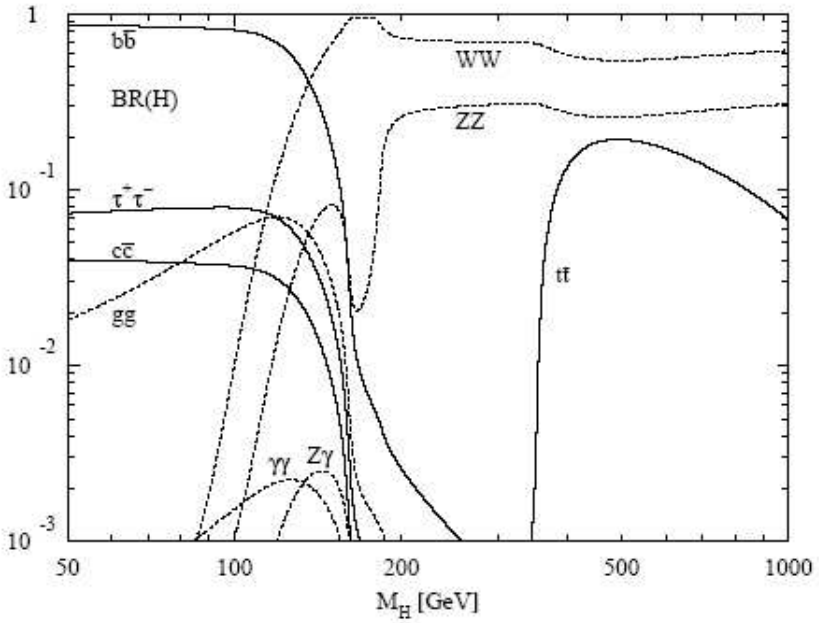

Figure 2.3.: Branching ratio of the Higgs boson as a function of its mass. Dominant decay channels for large masses are H$\longrightarrow$WW and H$\longrightarrow$ZZ. The decay products of these particles like ZZ$\longrightarrow \mu^+\mu^-\mu^+\mu^-$ have a distinct signature in the CMS detector [?].

3. The CMS experiment

3.1. LHC

Since the standard model predicts that the mass of the Higgs boson m_H could be several hundred GeV and the current accelerators cannot reach such energies, it was decided to build a new accelerator, the **L**arge **H**adron **C**ollider LHC, in the existing LEP[1]-tunnel at CERN[2] in Geneva. So far masses of the Higgs-boson of $m_H < 114,4$ GeV have been excluded by previous experiments [**?**]. Also no evidence for supersymmetrical particles has been found yet.

Starting in 2007, the LHC will operate at a center of mass energy of $\sqrt{s} = 14$ TeV and a luminosity of $L = 10^{34}$ cm^{-2}s^{-1} (high luminosity run). These energies of proton-proton-collisions should allow the production and detection of Higgs-bosons, assuming it exists.

The neutral Higgs-boson can only be detected indirectly by identifying the decay particles. Since the coupling of the Higgs-field to a given particle is proportional to the mass of that particle, the main decay channel will be the one producing the heaviest possible pair of particles (Figure 2.3).

The LHC facility will be used by 4 large collaborations, together with some smaller ones, to carry out their experiments. These major experiments are situated at 4 interaction points along the 27 km long ring, 100 m below the surface (Figure 3.1). They are called:

- ALICE[3]: studies of quark-gluon plasmas with a heavy-ion detector (point 2)
- ATLAS[4]: search for the Higgs-boson and supersymmetrical particles (point 1)
- CMS[5]: search for the Higgs-boson and supersymmetrical particles, similar to ATLAS (point 5)
- LHCb[6]: precise measurements of CP violation and rare decays (specialized in b-physics) (point 8)

[1] **L**arge **E**lectron **P**ositron collider
[2] **C**onseil **E**uropéen pour la **R**echerche **N**ucléaire
[3] **A** **L**arge **I**on **C**ollider **E**xperiment
[4] **A** **T**oroidal **L**HC **A**pparatu**S**
[5] The **C**ompact **M**uon **S**olenoid
[6] The **L**arge **H**adron **C**ollider **b**eauty experiment

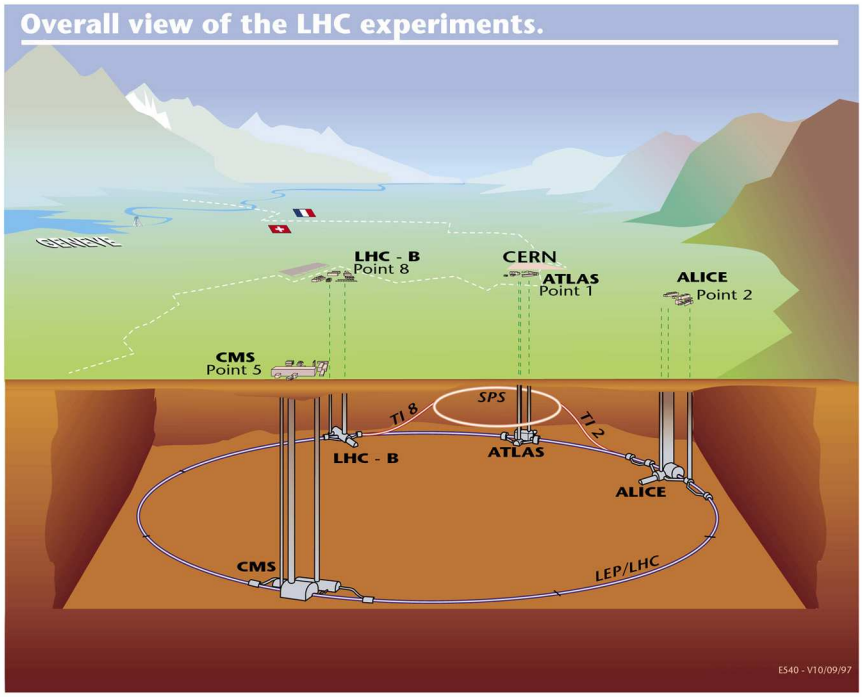

Figure 3.1.: Positions of the four major experiments in the LHC-tunnel at CERN, Geneva. Starting in 2007, they will carry out experiments regarding Higgs bosons and Supersymmetry (ATLAS and CMS), heavy ions (ALICE) and CP violation in the b-sector (LHCb).

3.2. CMS

The CMS detector (Figure 3.2) is a general purpose proton-proton detector, which is built, like all modern detectors, symmetrically around the interaction point with cylindrical (barrel) parts and endcaps. The energy of particles, created at the interaction point, is measured by the electromagnetic and hadronic calorimeter. The track of charged particles is bent by a ca. 4 Tesla strong magnetic field. This makes the measurement of their momentum possible. The magnetic flux outside the solenoid magnet is led back by an iron yoke which also houses the muon system. All components together have a length of 21.5 m, a height of 15 m and a total weight of 12,500 tons. Along the beam axis (z-axis), the detector is composed of 5 separate wheels, which allows better access to all detector parts during construction and maintenance. Starting at the interaction point and going outwards, these components can be described in the following order:

- Closest to the beam axis is the Tracker. It consists of silicon pixel (inner tracker) and silicon strip (outer tracker) detectors which allow the reconstruction of vertices with a resolution of 10 μm and 40 μm respectively. The relative resolution for the measurement of the transverse momentum is $0.15 \cdot p + 0.005$ (p in TeV) for the central region. The high resolution of especially the inner tracker, allows the

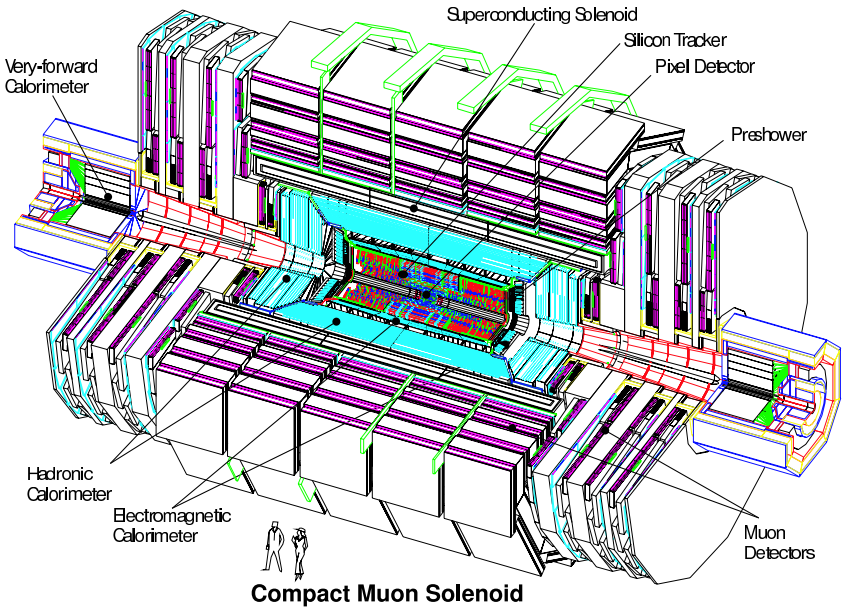

Figure 3.2.: Overview of the CMS detector with five wheels in the barrel region and two endcaps.

reconstruction of secondary vertices, created by the decay of short lived particles.

- The Electromagnetic Calorimeter (ECAL) is specialized in identifying electrons and photons and in measuring their energy. These types of "particles" cause electromagnetic showers in the over 80,000 $PbWO_4$-crystals with a total weight of over 93 tons. The length of the crystals of 23 cm corresponds to 25.8 radiation lengths and guarantees that the electrons and photons deposit all their energy in the ECAL. The intensity of the fluorescent light that is generated is proportional to the particle energy and is measured by avalanche photodiodes directly attached to the crystals. The distinction between electrons and photons is made by combining data from ECAL and Tracker, since only electrons produce a track in the latter. The energy resolution of the ECAL is less than 1% for energies above 100 GeV.

- The next component is the Hadronic Calorimeter (HCAL). Particles that interact strongly (hadrons) deposit most of their energy in this detector part because of the high density of the material. The HCAL is a so-called sampling detector, consisting of 50 mm thick copper plates interleaved with 4 mm thick scintillator plates. The copper causes hadronic showers through the interaction with passing particles. The photons created in these interactions are detected in the scintillator material. Measuring their energy indirectly measures the particle's energy. An energy imbalance ("missing transverse energy") can indicate a neutrino that has escaped direct detection because of its inertness.

A more or less invisible detector part is the "Trigger" system. The bunches of particles in LHC will collide at a rate of 40 MHz, resulting in over 10^9 interactions per second.

To be able to store data, this rate has to be reduced to 100 Hz. In several stages the initial rate is reduced by Triggers for each detector part and a global Trigger for the whole detector. These select interesting events and pass them on to higher Trigger levels. Eventually this has to lead to a rate at which data can be stored for later analysis.

Another system that is not directly related to detecting particle, but is important for track reconstruction, is the aligment system. This is divided into several subsystems for the detector parts and allows to determine the position of one part with respect to another. For the barrel muon system (described in the next section) it uses LEDs[7] on"alignment forks" as light sources. These forks (Figure **??**) are mounted on the chambers' honeycomb structures. The position of the LEDs is calculated from the light intensity distribution falling on CCD[8] cameras.

3.3. The muon system

The outer detector part, that is outside the superconducting coil, is almost entirely made up by the muon system, which is an important subsystem. Muons, that may originate from an important decay channel of the Higgs-boson ($H \rightarrow ZZ \rightarrow \mu^+\mu^-\mu^+\mu^-$) as seen in section 2.4, are the only charged particles that reach this detector part. They only lose energy by ionization when passing through the various detector parts, leaving a distinct signature. To identify these muons and measure their momentum, the muon system consists of three different kinds of detectors.

- Drift Tubes (DT) are used for a precise measurement of the position (momentum) in the barrel region. They will be described in more detail in the next chapter.
- Cathode Strip Chambers (CSCs) are multiwire proportional chambers that are better suited for the use in high and inhomogeneous magnetic fields, as is the case in the Endcaps. One cathode plane is segmented into strips running across wires. If an avanlanche develops on a wire, it induces a charge on several strips in the cathode plane. With this method, two coordinates are obtained from one detector plane. A spatial resolution of 50 μm can be achieved, which is not affected by the composition, temperature and pressure of the gas[**?**].
- Resistive Parallel plate Chambers (RPCs) are used in both the barrel and the endcap region. These gaseous detectors have a good spatial resolution and a high time resolution. They consist of two parallel plates of resistor material (bakelite) separated by a gas gap of a few millimeters. The outer surface is coated with graphite paint to form the high-voltage and ground electrodes. The electric charge that results from an avalanche drifts towards the anode and induces a charge on a pick-up electrode, which is the signal used in the RPCs. This structure is capable of tagging the time of an ionizing event in times shorter than the 25 ns between two bunch crossings and is therefore well suited for fast space-time tracking as required for the muon trigger[**?**].

[7] Light Emitting Diodes
[8] Charge-Coupled Device

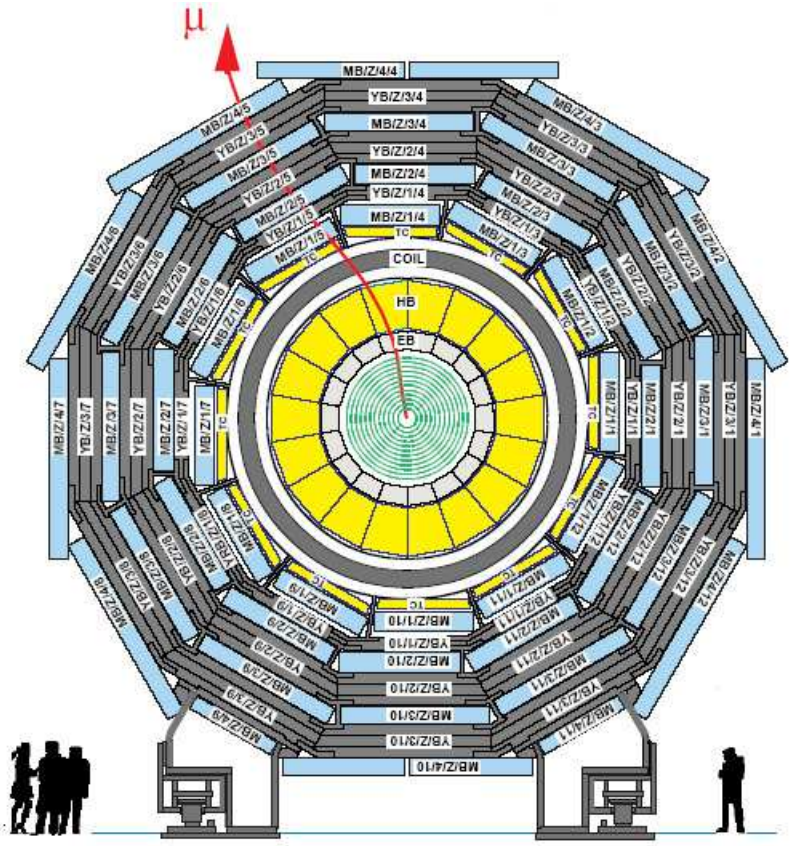

Figure 3.3.: View of the CMS detector along the beam axis. The Tracker in the center (green) is followed by the ECAL (light gray), the HCAL (yellow), the magnet coil (gray) and finally the muon system (light blue) embedded in the return yoke (gray). The track of a muon flying through the detector is indicated by the red arrow.

3.3.1. Drift Tubes

The muon system in the barrel region is embedded in the iron magnet return yoke. There are four stations where position and momentum of a muon are measured by one muon chamber each. The chambers essentially vary only in size, with the smallest so-called MB1-chambers[9] near the center of the detector and the largest (MB4) on the outside.
The III. Physics Institute A of the RWTH Aachen is manufacturing 60 MB1-chambers and 10 MB4-chambers. The other chamber types are produced by institutes in Madrid (Spain) (MB2), Legnaro (Italy) (MB3) and Bologna (Italy) (MB4).

An MB1-chamber has the dimensions 1990x290x2536 mm and is composed of 3 so-called Super Layers and a honeycomb structure for robustness. Each Super Layer is made of 4 layers of parallel positioned drift cells, while each layer is shifted half a cell with

[9] first station of **M**uon **B**arrel chambers

respect to its neighbors above and/or below. This is done to resolve tracking ambiguities. To enable the measurement of the momentum in both angular coordinates ϕ and θ the middle Super Layer ("θ-layer") is rotated 90° with respect to the other two ("ϕ-layers"), as shown in Figure 3.4. The other purpose of the honeycomb structure, besides giving stability, is the use as spacer between the Super Layers.

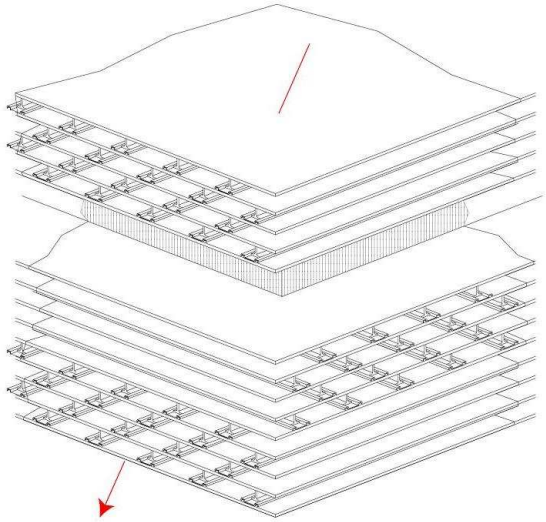

Figure 3.4.: Schematic arrangement of the 2x4 layers of the ϕ-layers (upper and lower) and 1x4 layers of the θ-layer (middle). The honeycomb structure that gives the chamber stability and improves momentum measurement in the ϕ-coordinate is not shown here.

Each layer contains 50 to 58 cells, depending on the type of Super Layer. Between two layers there is a 2 mm thick Al plate, between two cells in a layer there is a 2 mm thick "I-beam". One such cell (Figure 3.5) is 42 mm wide, has a height of 11 mm and stretches the full length of the Super Layer. An anode wire, connected to a voltage of +3600 V, is positioned in the center of each cell. Glued onto the I-beams are two cathode strips, connected to a voltage of −1200 V. To optimize the electric field form in the cell, field-forming anode strips are glued to the plates between the layers. These are connected to a voltage of +1800 V. This results in an electric field that is as homogeneous as possible.

The chosen geometry, gas mixture and parameters for high voltage restrict the intrinsic absolute spacial resolution of one drift cell to 250 μm. The combination of data from all 12 layers improves this to 100 μm for a whole muon chamber. These errors in measuring the coordinates, together with errors in magnetic field strength and in the measurement of vertices, yields a momentum resolution of

$$\frac{\Delta p}{p} = 10\% \cdot p[\mathrm{TeV}] \oplus 8\%$$

for the CMS detector as a whole.

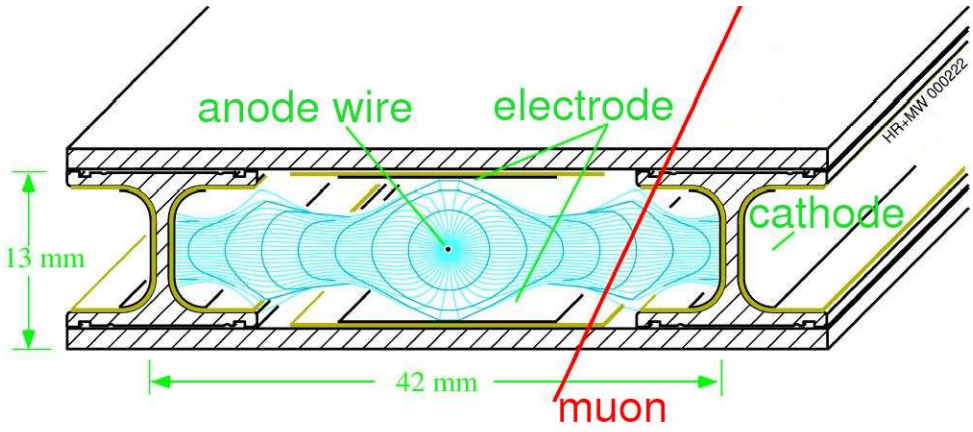

Figure 3.5.: Drift cell of a CMS muon chamber. The anode wire in the center has a voltage of +3600 V. The cathodes, glued to the I-beams have a voltage of −1200 V. The field-forming electrodes on the top and bottom plate (+1800 V) make the electric field as homogeneous as possible.

3.3.2. Operation principle and drift velocity

A muon passing through a drift cell (Figure 3.5) generates ion-electron-pairs along its path by ionizing the gas. Due to the high electric field between the cathode strips and the anode wire the electrons are accelerated towards the wire in the center of the cell while the ions drift towards the cathode strips on the I-beams. The balance between acceleration and collision of the electrons with the gas atoms leads to an almost constant drift velocity u for the electrons throughout the drift cell except close to the anode wire where the electric field increases rapidly. Here the electric field is proportional to $\frac{1}{r}$ while in the main drift volume the electric field is almost constant. In the vicinity of the wire the electrons gain enough kinetic energy to ionize atoms on their path which gives rise to electron avalanches. A measurement of the drift time yields the position where the muon passed through the cell. Combining this information with time measurements from other drift cells allows the reconstruction of the muon track.

As shown in [?], the drift velocity u depends on E/p (Figure 3.6). A value for E/p should be chosen that leaves u practically unaffected for small variations of E/p. As can be seen in Figure 3.5, the electric field is not perfectly homogeneous and also variations with time cannot be excluded. To prevent variations of the gas pressure p from adding to those of E, the pressure must be kept as constant as possible, thereby keeping u as constant as possible.

The properties of a drift cell, in particular the drift velocity of the electrons, depend on the high voltage applied to anode and cathode and on the properties (mixture and pressure) of the gas inside. The mixture of the gas means the fractions of gases that improve the electron avalanches (amplification) and those that counter the amplifying effect (quenching). Quench gases are usually organic gases that have more degrees of

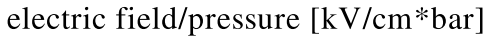

Figure 3.6.: Dependence of the drift velocity on E/p. The stars represent measured data points, the curve is the result of simulations with a gas mixture of Ar/CO_2 (85%/15%) [**?**]. By optimizing E/p, the drift velocity will be unaffected by small variations. The optimum is found at $(E/p)_{nom} = 1.1$ kV/cm · bar where the drift velocity u_{nom} is 55 μm/ns.

freedom than inorganic gases. They therefore have a better chance of absorbing photons that are emitted together with electrons and that could otherwise cause more unwanted avalanches. This thesis is about the measurement of the gas pressure in the muon chambers and more specifically about the read-out-boards, so-called PADC[10] boards that are used.

3.3.3. Construction of the muon chambers

The construction of a MB1 muon chamber starts with an aluminum bottom plate equipped with field-forming strips, placed on one of four construction tables in the assembly hall of the physics institute. The I-beams that form the walls of the drift tubes are glued on top of that. Then the anode wires with crimp blocks holding both ends are inserted and the first layer of drift tubes is closed with a second aluminum plate which also acts as the bottom plate for the next layer of drift tubes. This is repeated three times to produce the four layers that make up a Super Layer. At the end of the mechanical production two frames are attached at both open ends of the Super Layer which will hold two removable covers. In the next step the Super Layer is equipped with High-Voltage-Boards (HVBs), distributing the various voltages to the anode wires, the cathodes and the field-shaping strips, and with Front-End-Boards (FEBs), having the

[10] **P**ressure **A**nalog to **D**igital **C**onverter

task of producing accurate timing signals from the electron signals picked up by the anode wires. HVBs and FEBs are both enclosed in the gas volume of the Super Layer.

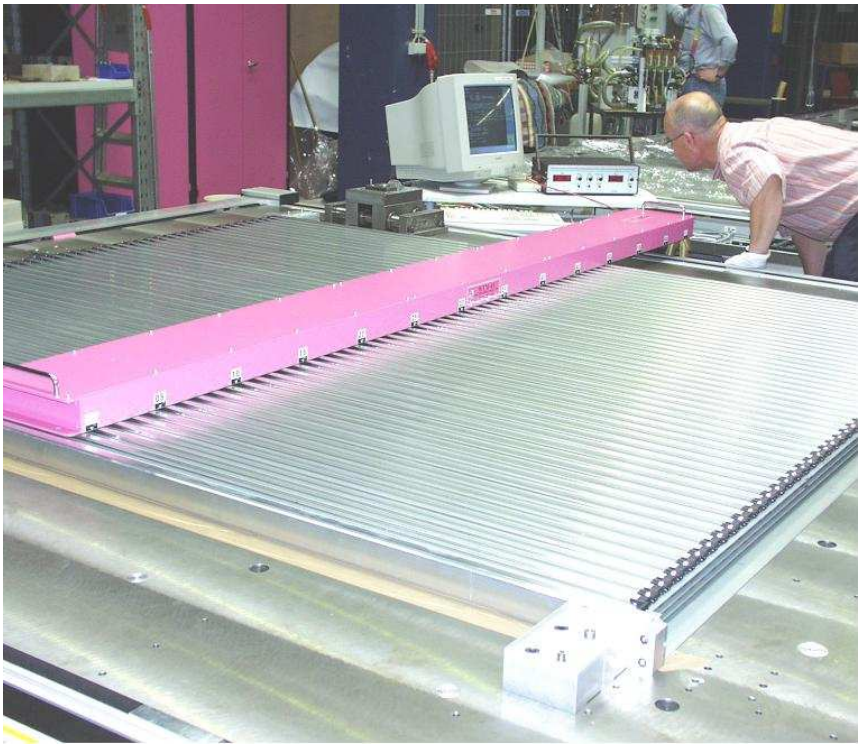

Figure 3.7.: One of the tests that is done for every layer of wires is a measurement of their mechanical tension. Via a contactless measurement of the resonance frequency, the mechanical tension of every wire is determined.

After the Super Layer has been mechanically finished and all electrical components have been added, it is closed on either side with a cover. One cover (HV-side) has plugs to connect the anode wire, the cathodes and the strips to high voltage, the other cover (FE-side) has plugs for the read-out of the data and connections for the water-cooling. Both covers are also used for the gas distribution within the Super Layer. One θ- and two ϕ-Super Layers as well as a honeycomb structure are glued together to produce a finished muon chamber.

In every stage of production the chamber parts are subject to measurements and test for Quality Control. These include the measurement of the mechanical tension (Figure 3.7) and position of the anode wire, HV tests in air and gas and tests for gas tightness. The functionality of a whole muon chamber is tested in a specially built test stand, where data are taken with muons from cosmic rays (Figure 3.8).

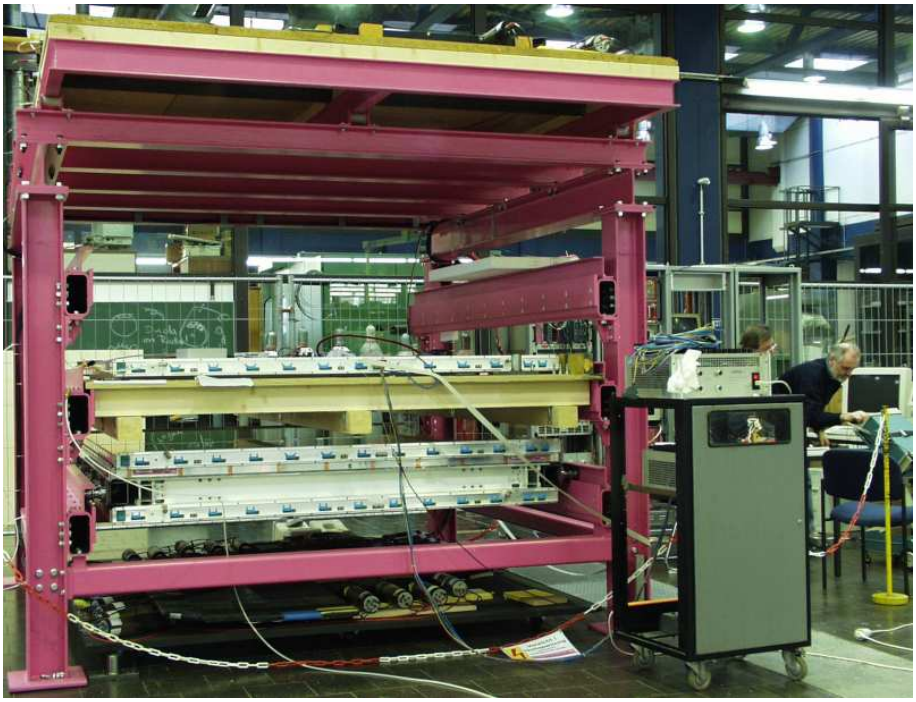

Figure 3.8.: The test stand in Aachen. Muon chambers and single Super Layers are tested with muons from cosmic rays.

4. Gas system of the muon chambers

4.1. Gas properties

The gas that is used in the muon chambers of CMS has to flush every drift tube with controlled temperature, pressure, flow and purity and has to meet a number of requirements. The gas has to be inflammable and relatively cheap considering the total volume of the muon chambers (ca. 1 m^3 per chamber). Also organic components are unwanted because of depositions of polymers on the anode wire. The gas that was chosen is a mixture of Ar/CO_2, Ar being the amplification gas and CO_2 being the quench gas. Tests showed that the concentration of the CO_2 has to be more than 10% in order for the quenching process to work and less than 80%, depending on the geometry of the drift cells. For CMS a ratio of 85% Ar to 15% CO_2 was chosen.

The nominal operating gas pressure will be about 10 mbar above ambient pressure. This value is chosen for several reasons. One reason is to make sure that no air (O_2 and N_2) can get into the muon chamber through a leak. Only a small overpressure is used, because otherwise the force on the chamber's top and bottom plates would become too large and the chamber would explode. This is due to the large surface area of the top and bottom aluminum plates of the muon chambers. From $F = p \cdot A$, with F being the force, p the pressure and A the area, it follows directly that with an area of $4\ \text{m} \cdot 2.5\ \text{m} = 10\ \text{m}^2$ for the largest version of the muon chambers, the pressure (in this case overpressure) must be kept small in order to guarantee that the glue between the aluminum parts can keep the whole structure together. The chambers are built to withstand a pressure of 100 mbar above ambient pressure.

4.2. Gas distribution

The gas, which is mixed in a purpose-built facility, is distributed to the 250 muon chambers in the barrel region through a closed circuit of pipes, manifolds and valves. First the gas is distributed to the 5 wheels of the detector, one of which is shown in Figure 4.1. After this has happened at ①, the gas flows through 100 m long pipes to a distribution panel ② on every wheel, where the next branching to the 50 muon chambers of each wheel takes place. Arriving at a muon chamber, the gas flow is split into three separate ones, one for each Super Layer, by a gas manifold ③ that also houses two pressure sensors. One such manifold at the inlet and one at the exhaust of a chamber makes a total of four sensors that constantly monitor the pressure inside. The final branching takes place inside every Super Layer ④ and distributes the gas homogeneously to the 200 to 400

drift cells per Super Layer by a tube with a hole in front of every drift cell.

To ensure that air can be removed from the chamber, even at small gas flow, the inlet of the Ar/CO_2, which is denser than air, is always in a corner on the lowest side of the chamber. The exhaust lies at the opposite corner on the highest side so the gas has to travel diagonally through the Super Layer, pushing out any air. The quality of the gas with respect to residual air is determined by measuring the amount of oxygen it contains. This amount should be less than 500 ppm.

After the gas has passed through the drift tubes, it is collected and reunited with gas from the other muon chambers in reversed order of the previous description. This will take the gas back to the mixer room at the surface with a gas flow of 50 l/h under normal operating conditions, corresponding to a few volume exchanges per day. In every cycle 10% of the gas will be replaced.

4.3. Measuring and monitoring

The muon chambers will be filled with gas during the experiment but also during tests in the production sites. For a number of reasons the gas pressure has to be measured and monitored during both test stage and experiment.

- The drift velocity of the electrons in the drift cells depends on E/p, E being the electric field and p the gas pressure. Both E and p may very slightly without affecting the drift velocity (see Figure 3.6 in section 3.3.2). The pressure therefore has to be monitored, so that larger variations that do affect the drift velocity, can be detected.

- The muon chambers in CMS will not all be exposed to exactly the same gas flow and pressure due to a pressure drop caused by the length of the piping and the barometric difference. Still the gas flow should be locally constant. By verifying that the pressure inside a chamber is constant, one has indirect evidence that also the gas flow is constant.

- As mentioned earlier, the chambers can withstand a pressure of 100 mbar above ambient pressure. To prevent it from exceeding this limit, the pressure must be constantly monitored, so that in such a case, appropriate action can be taken.

- For the purpose of quality control, all chambers are tested for gas tightness. If the gas pressure cannot be maintained for a certain period of time, due to leaks, this would lead to an unnecessary large consumption of gas, which would in turn be too expensive.

4.4. The monitoring system

A number of devices is used to measure and monitor the pressure of the Ar/CO_2 during the experiment stage.

4.4.1. sensors

The first device needed to measure the pressure is of course a pressure sensor. The sensors that are to be used have to meet a number of requirements.

- The sensors have to be small in order for two sensors to fit into each of the two gas manifolds per muon chamber. Since there already is not much room for the manifolds to be mounted onto a chamber, the room inside a manifold is limited to a few cm^3. By using small sensors and thus more than one sensor per manifold, there will be enough redundancy to tell erroneous sensors apart from pressure variations, as the latter will be noticed by at least two sensors.

- With 4 sensors per chamber and a total of 250 chambers plus some spare chambers and spare parts, this adds up to quite a large number. Considering that the production sites will also need sensors for test purposes, the conclusion is that the sensors have to be relatively cheap.

- For the experiment, the range of the sensors does not have to be very large, but during gas tightness tests the sensors have to be able to measure an overpressure of 100 mbar and more. However, since the overpressure in the experiment is ca. 10 mbar, the accuracy of the sensors has to be ca. 1 mbar to make a sensible measurement possible.

- In principle there will be no direct access to the sensors over longer periods of time. They therefore have to be able to submit data in electronic form. This also makes it easier to register the data during the experiment as well as during tests.

- The CMS experiment will run for ca. 10 years. The lifetime of the sensors should therefore be more than 10 years.

- The sensors have to withstand the magnetic field of the solenoid magnet as well as a very high radiation.

Regarding these requirements, 2 types of sensors were chosen from a choice of products. These are the *MPX2050DP* and the *MPX2010DP* from *Motorola* for the measurement of a differential pressure (the difference in pressure between the two inlets of the sensor) of ±500 mbar and ±100 mbar respectively. The functional principle of these sensors (Figure 4.4.1) is that the pressure on a silicone die coat is transmitted to a membrane which is connected to a quartz crystal. The resistance of this crystal, to which a voltage of 12 V is applied, changes proportional to the exerted pressure through the piezoelectric effect. This then changes the output voltage from 1 mV when no pressure is exerted to a maximum of 58 mV. Because this is a rather small voltage, these signals are amplified and eventually have a range from 0.3 V to 4.3 V when they arrive at the read-out device.

The sensors are designed to withstand a differential pressure of 750 mbar, have short response times (ca. 1 ms) and can operate in a large temperature range. But the inaccuracy can reach up to 20% over the total pressure range, which corresponds to ±25 mbar for the MPX2050DP and ±5 mbar for the MPX2010DP. Also it was found that the offset

output voltage (when the pressure difference is 0) can vary from sensor to sensor by 10%. To eliminate these uncertainties and determine the actual (in)accuracy, it was decided that every single sensor had to undergo a calibration.

During a calibration cycle one of the sensor's inlets always measures the ambient pressure, the other one is exposed to the pressure of the gas, which continually rises from ca. -600 mbar to ca. $+600$ mbar relative to ambient pressure. The reference pressure is given by two Baratron devices[1], one of which measures ambient pressure while the other one is connected to the gas. The output signal of these devices is the same in Volt as the pressure that is measured. The output voltages of all devices are digitized by 16-bit ADC-chips on two NI6014-boards by National Instruments and written to a text file by a LabVIEW program.

The calibration rack, which is shown in Figure 4.3, allows for the simultaneous calibration of up to 10 manifolds (20 sensors). With so many sensors being calibrated per cycle, there is enough redundancy to rule out misinterpretation of the sensor signals (e.g. atmospheric pressure variations noticed by all sensors) and it shortens the total time needed.

The calibration runs are carried out by H. Lampe, who does all the connecting and disconnecting of the gas manifolds and runs the LabVIEW program. The evaluation of the data, resulting in a calibration report with plots for all sensors (Figure 4.4), is then done by Dr. H. Reithler. An additional LabVIEW program, developed by F. Lanzerath uses the calibration data to make a lookup table for every single sensor. In this table the output voltages of the sensor are matched to the reference pressure. This will be used in the experiment to determine the actual pressure in the muon chambers.

4.4.2. Read-out electronics

Since the data from the pressure sensors are presented as output voltages, a read-out system that can handle these signals is needed. The so-called Pressure Analog to Digital Converter board, or PADC board, like its name says, converts the analog signals from the pressure sensors into digital values that can be processed by a computer. A more detailed description will be given in chapter 5.

4.4.3. MiniCrate

The next link in the pressure-data chain is the so-called MiniCrate mounted on the HV-side of every muon chamber. It acts as the housing for the first part of the DAQ[2] system, the 1st-level muon trigger and parts of the DCS[3]. So the MiniCrate is the chamber's link to the outside world, as illustrated in Figure 4.5. One of the tasks of the DCS components inside the MiniCrate is the read-out and control of the PADC board. The communication between MiniCrate and PADC board uses the I^2C-protocol, created by

[1] two *390 HA-10000SP05* devices made by *MKS Instruments Inc.*
[2] Data Acquisition
[3] Detector Control System

Philips. This I^2C-bus (see section 5.2) is a serial bus that is often used if there is no need for high-speed communication.

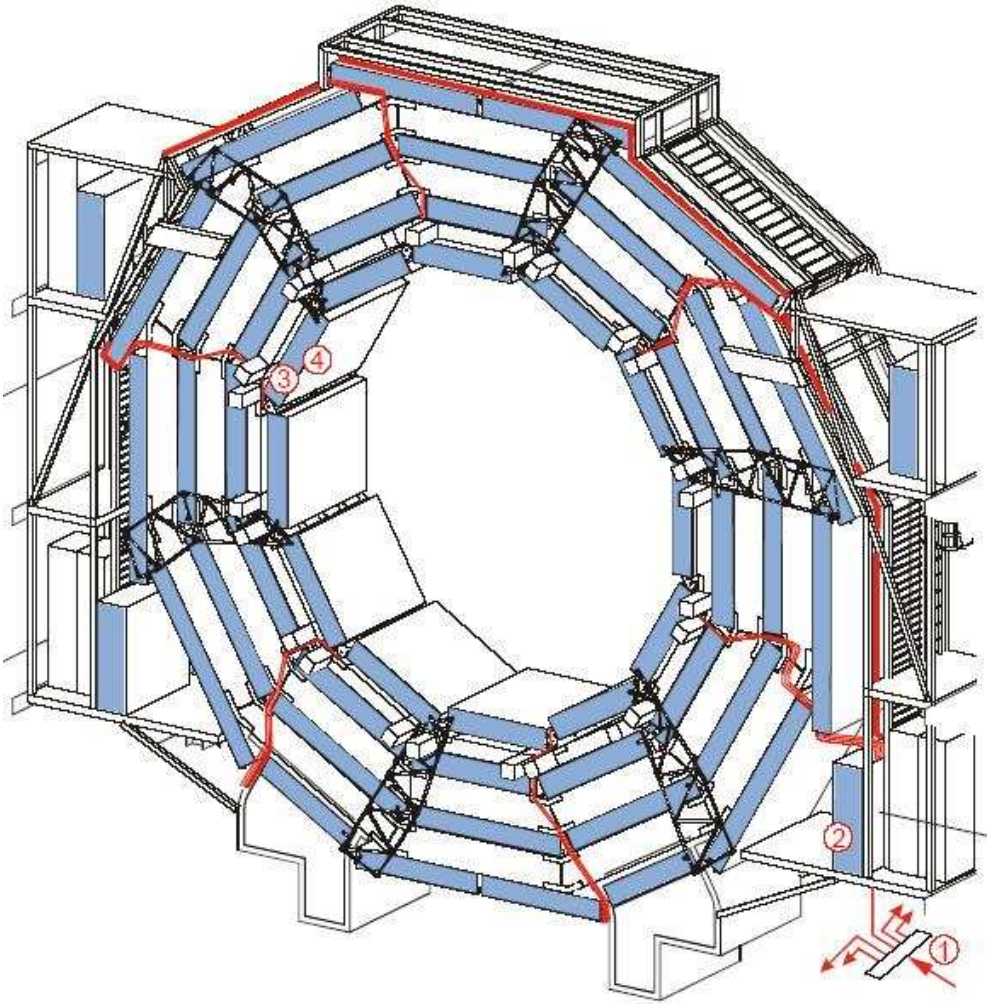

Figure 4.1.: The gas distribution system of one of the five wheels. After the gas has left the mixer room at the surface it will be divided into smaller portions 4 times before it arrives in the drift cells.

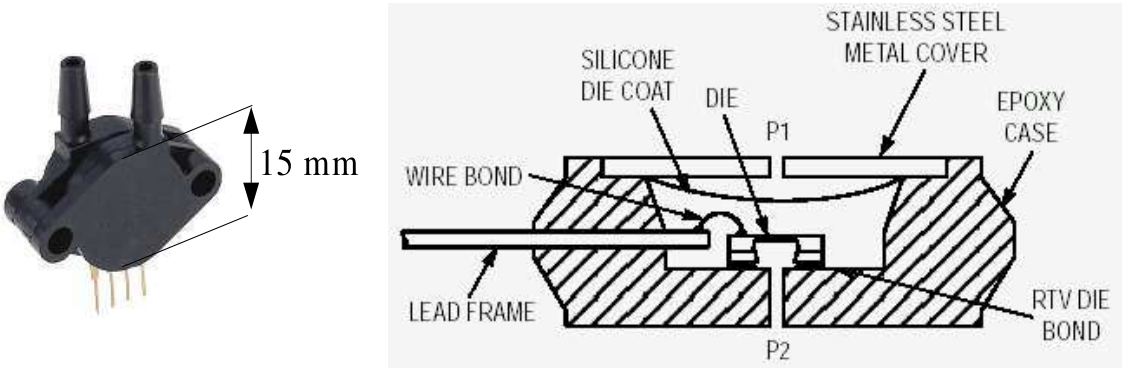

a) b)

Figure 4.2.: a) A pressure sensor that is used for measurements at the muon chambers. b) Schematic view of a sensor. Pressure exerted on the quartz crystal changes its resistance and thereby the output voltage.

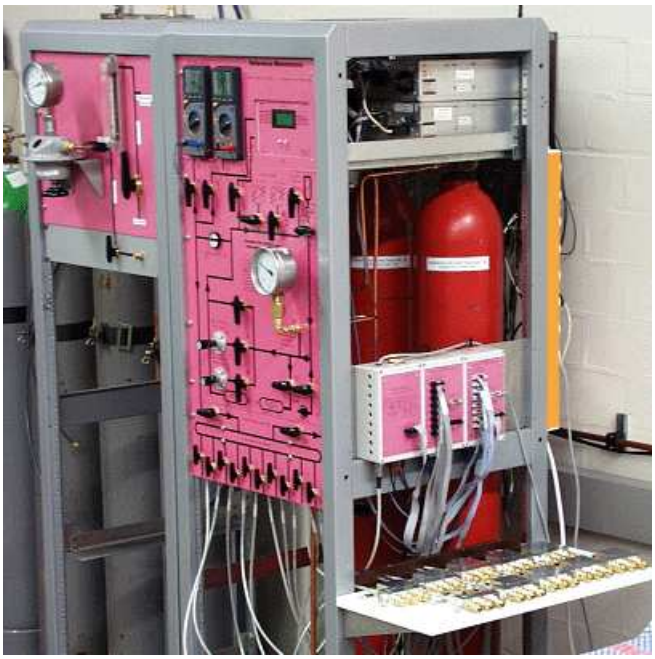

Figure 4.3.: The gas teststand, used for the calibration of the pressure sensors. The manifolds, up to 10 per cycle, are placed on the white plateau in the lower right corner.

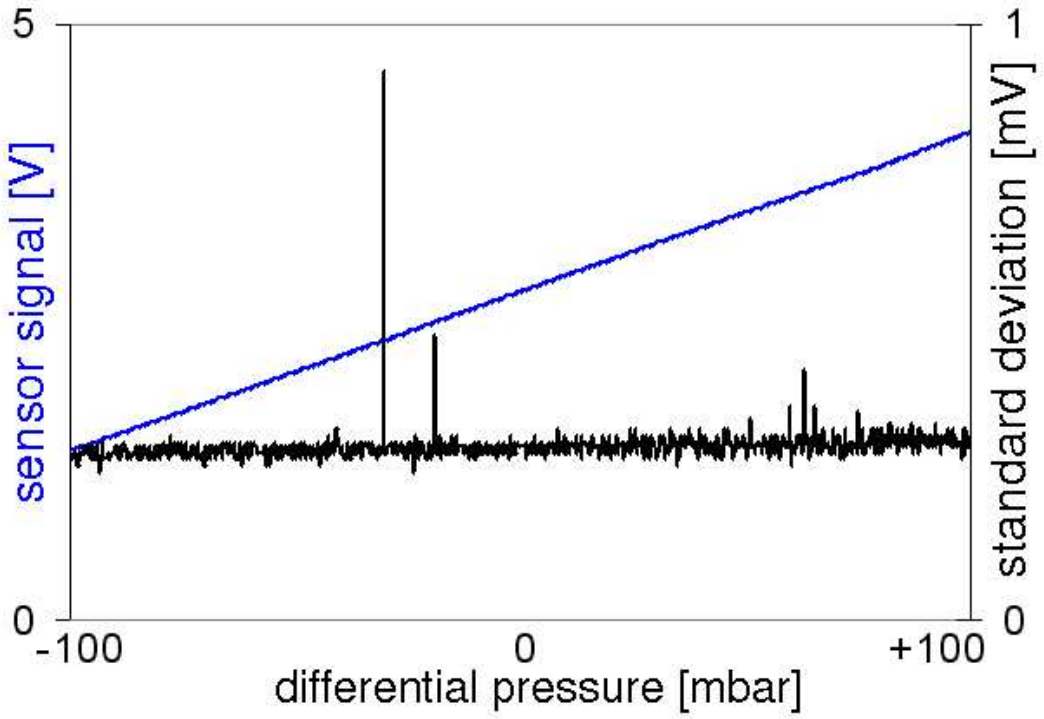

Figure 4.4.: The calibration of the pressure sensors results in a correlation between the output voltage of the sensors (left vertical axis) and the reference pressure (differential pressure). One point is the average of 1000 measurements. The standard deviation (right vertical axis) is smaller than 1‰.

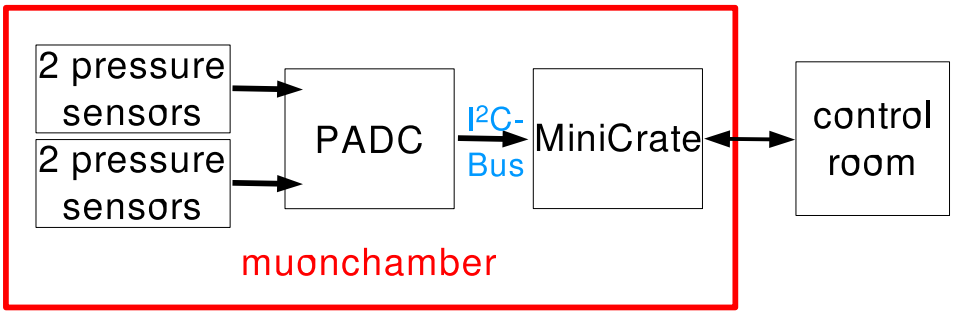

Figure 4.5.: Schematic read-out system for the gas pressure: 2 pressure sensors per manifold are read out by 1 PADC board. The digitized data are transmitted to the MiniCrate and then to a computer in the control room.

5. Readout board for the pressure system

5.1. Initial concept

The original idea was to have a read-out board for the pressure data that had a microcontroller (mc), EEPROM[1] and an ADC. The microcontroller runs a program that tells the ADC to continuously digitize the analog data. The microcontroller monitors these readings and writes the average value, measured during a few minutes, to the EEPROM. The data written to EEPROM is the pressure in mbar, which is calculated by the microcontroller using the calibration tables of the sensors stored in the EEPROM. If a request for data comes over the I2C-bus, it is this average pressure that is transmitted. The microcontroller can also set a flag (alarm) when the pressure exceeds the permitted range.

A configuration like this would have a number of advantages. Data would be taken autonomously and transmitted when needed. All sorts of calculations can be done by the microcontroller as long as the calibration tables loaded into the EEPROM are the correct ones. No allocation tables to determine which devices are mounted on a muon chamber would be needed, eliminating a source of errors.

The PADC board has to pass a number of tests before it is going to be used in the experiment. First of all, it has to be able to carry out the task it is designed for: digitize the sensor signals and transmit the data to the outside world. Then it has to endure radiation hardness tests and tests in a magnetic field. Finally a temperature test is carried out. These tests are necessary because of the environment the board is going to be in during the experiment.

5.2. Communication with the PADC board

The readout of pressure data is done via the *Inter-IC bus*, or I^2C-bus, mentioned earlier. This is a serial bus, developed by *Philips*, that can be used in various environments because of its robustness and flexibility. It is easily expandable and needs little wiring. To meet the demand for higher speeds, the original 100 kbit/s (normal mode) have been upgraded to 400 kbit/s (fast mode) and 3.4 Mbit/s (high-speed mode), but in many applications ("slow control") high speeds are not required.

The data signal line (SDA[2]) and clock signal line (SCL[3]) are the two bi-directional

[1] **E**lectrically **E**rasable and **P**rogrammable **R**ead-**O**nly **M**emory
[2] **S**erial **DA**ta
[3] **S**erial **CL**ock

lines needed for this multi-master bus. Every device on the bus can, in principle, act as master or slave and as transmitter or receiver. To avoid confusion, data loss and blockage, there may be only one master at a given time. The master gains control over the bus by "pulling" the SDA-line, whose level is at +5 V (high) when not busy, down to 0 V (low). All other masters that were trying to gain control, will now have to wait until the bus is free again. The master can communicate with slaves by using the 8-bit (sometimes 10-bit) address that is unique for each device.

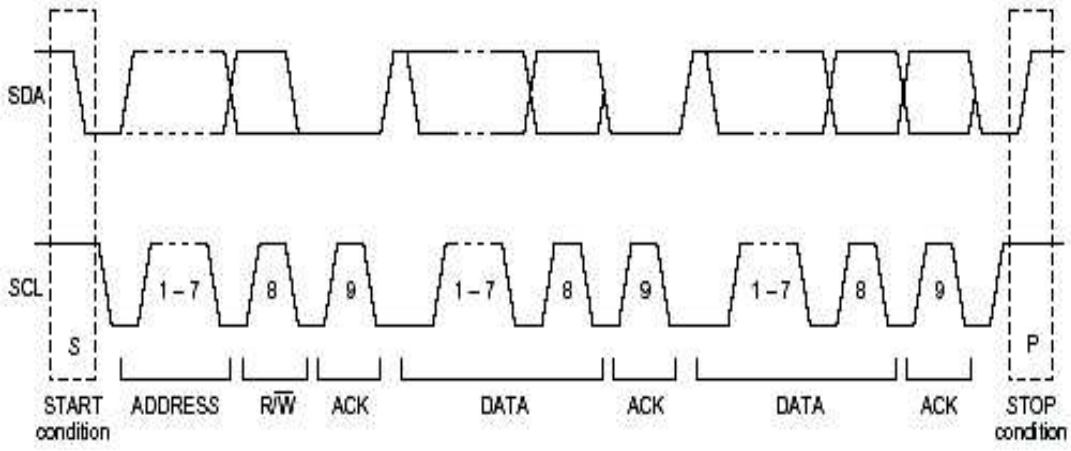

Figure 5.1.: A complete I^2C data transfer with the transitions between High and Low of the SDA and SCL line, the numbers representing the number of bits needed.

An example of the I^2C-protocol is shown in Figure 5.1. A master pulling the SDA-line low, when the SCL-line is high, issues a "Start" condition. It now controls the bus and can start data transfer. The Start condition is followed by the address of the slave it wants to communicate with. A slave recognizing the address then issues an "Acknowledge" (Ack) after which the master can write to or read from the slave or a combination of both. After data transfer, the master releases the SDA-line (Stop condition), making it possible for other masters to gain control.

To get acquainted with the I^2C-protocol, I used the parallel port of a laptop with a device made by Prof. Hebbeker. Two pins of the port were used to simulate the SDA and SCL line. To communicate with the actual read-out board(s) two other devices were tried. The first was a device for communication with I^2C slave devices via the RS232-port of a computer. The software, translating short commands of letters into I^2C-commands, was designed by F. Beissel and H. Szczesny. This is the device that eventually was used in all tests in Aachen and in the calibration of the boards. For these purposes a software was developed in *LabVIEW* that sends the strings needed for the read-out automatically to the translator-device, rather than having to send them manually one by one. LabVIEW is a graphical programming language with the main purpose of controlling hardware. The user designs a workspace that looks like ordinary instruments with switches and displays and which is therefore called *Virtual Instrument (VI)*. The logical connections are made in a *block diagram* in the background.

The second device was similar to the first one. It is a USB-I^2C-interface that translates strings sent by the USB[4] into I^2C-commands (internally USB-RS232-I^2C) and vice versa. This board and software were designed by colleagues of the Atomki[5] in Debrecen, who used it in their work on the alignment forks of the muon alignment system that uses the same I^2C-bus as the PADC. Due to problems we experienced in the communication via this device, we decided to go back to using the RS232-I^2C-device.

5.3. Versions of the PADC board

5.3.1. PADC board with microcontroller AT90S8535

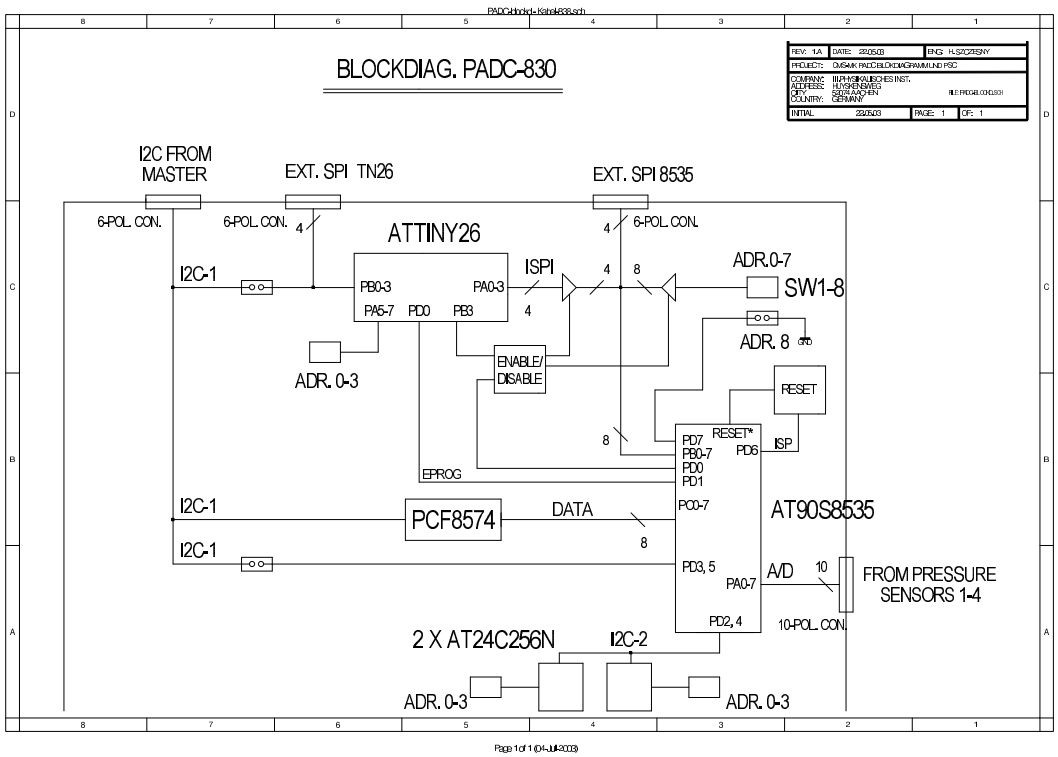

Figure 5.2.: Block diagram of the PADC board with the AT90S8535 chip. The main components besides the microcontroller are the ATtiny26 and the PCF8574.

The block diagram of the first version of the read-out board is shown in Figure 5.2. It has all the desired components described above (5.1). The microcontroller is the *AT90S8535*, made by *Atmel*, a 10-bit ADC with 8 channels and 8 kb of memory for program code. The programming was done via SPI[6] port of the chip that was connected

[4] **U**niversal **S**erial **B**us
[5] Institute of Nuclear Research of the Hungarian Academy of Sciences, Debrecen, Hungary
[6] **S**erial **P**eripheral **I**nterface

to a computer by a *STK500* board from Atmel. This board had been used in previous successful tests in which the chip controlled some LEDs. Later on the programming would have to be done via another small microcontroller (*ATtiny26* from Atmel).

Because there was no built-in two-wire interface (I^2C), a component was added to the design to make sure that the chip would not be constantly busy with bus-protocol, leaving only little time for digitizing signals. This *PCF8574*, made by *Philips*, has a I^2C-bus interface on one side and a 8-bit quasi-bidirectional port on the other, as well as an interrupt line ($\overline{\text{INT}}$) that can indicate traffic on the I^2C-side. The interrupt line was not connected to the interrupt logic but to a normal I/O-pin of the microcontroller. An $\overline{\text{INT}}$-signal would not interfere with the program, but would be noticed between the conversions after which the appropriate task could be carried out.

Unfortunately, the PCF8574-device did not work the way we thought it would. A number of tests showed that $\overline{\text{INT}}$ was set when the I/O-port of the AT90S8535 switched from input to output and that the parallel port of the PCF8574 had a value of x00 (hexadecimal notation, indicated by the x). The port and interrupt line could be cleared by reading out and sending a Stop condition. Then the microcontroller could send real data, which would set the $\overline{\text{INT}}$, and wait for it to be cleared again. This procedure is quite complicated and time-consuming, but it would work.

Another problem arose, when we tried to give the microcontroller the command to send one byte, depending on the command, then switch the port to input-mode to receive a second command and finally send a second byte. The microcontroller was e.g. programmed to send x6F if it received x11 and to send x89 if it received x32. We had success in getting the "right answer" on the first command, but the second "answer" would depend on what the previous value of the parallel port had been. We found no way to avoid collisions of this kind and often even had to reset the PADC board and the translator board because of a blockage that could not be solved. This also happened during the magnet test (section 5.5).

Meanwhile, our colleagues from Debrecen had been testing the pin-compatible successor of the AT90S8535, the ATmega8535, which has a built-in I^2C-interface. This would enable it to operate the I^2C-bus, without an extra load on the microcontroller and without the need for the PCF8574. They had shown that it could be (re)programmed via the I^2C-bus, which was one of the criteria for mass production. They also had success in the read-out of data, which was confirmed in Aachen.

We had to give up this version of the PADC board in the end, because apart from the changes in hardware on the boards, there was a lot of work needed on software development, like storing data and calibration tables in the EEPROM and use them for calculations. This could be done, but would simply take too much time to finish.

5.3.2. PADC with ADC MAX127

The second design that was tested, was one with an ADC that had a built-in I^2C-bus interface. This was the *MAX127* from *MAXIM*, a 12-bit ADC with 8 analog input channels. It was considered as an alternative when the problems with the first design remained, and was a serious candidate for mass production. The design of the board

as a whole was simpler because with the hardware I^2C-bus, there was no need for the PCF8574 and also no software had to be downloaded to the chip, making the ATtiny26 obsolete.

With respect to communication via the I^2C-bus, this design was easier to use, since all the MAX127 can do, is transmit data on request. Despite small problems, this was under control.

The problems that occurred during the magnet test (5.5), followed from the fact that this chip was not designed for an input range of $0 - 5$ V. Therefore an extra amplifier would be needed to adjust for impedance differences between the output of the pressure manifolds and the input of the ADC channels. This design was therefore also abandoned.

5.3.3. PADC with ADC MAX1138

The design of this board is similar to the previous one. The *MAX1138* from *MAXIM* is a 10-bit ADC with 12 analog input channels and a hardware I^2C-bus. Since this design was chosen for the mass production, the "PADC1138 board Nr. 852" will be described to more detail (Figure 5.3).

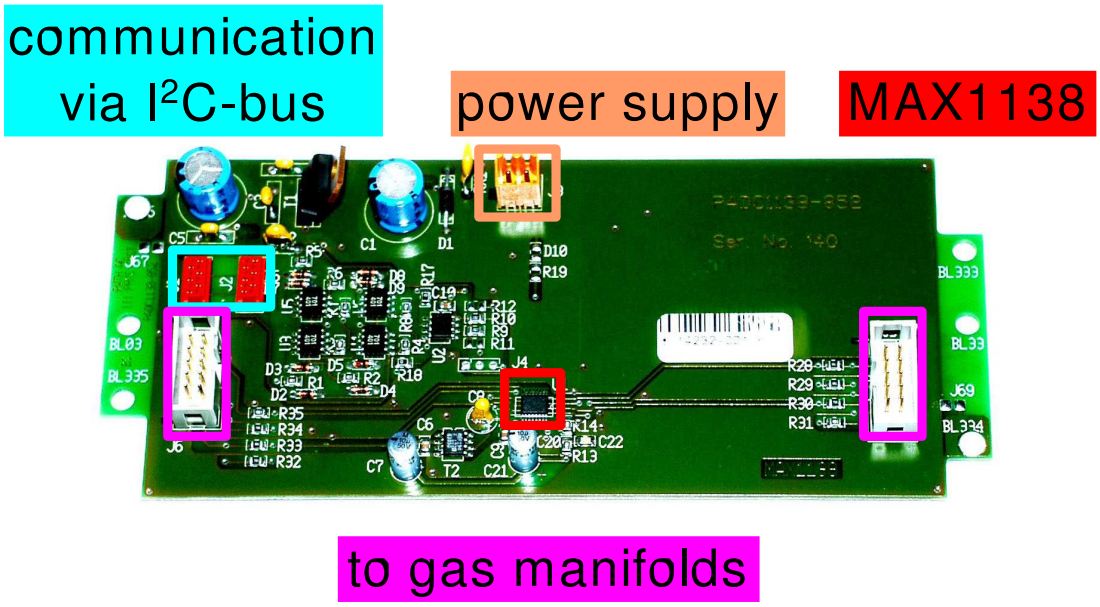

Figure 5.3.: The PADC board with the MAX1138 chip. Indicated with different colors are the chip itself (red) and the connectors to the gas manifolds (pink), the I^2C-bus (cyan) and the power supply (orange).

The PADC board together with the two gas manifolds per chamber have a power supply of +6 VDC on connector J3 (the orange connector in Figure 5.3). A voltage stabilizer supplies the ADC with +4.5 VDC. A voltage of +5 VDC is used for the power supply of optocouplers that isolate the board's circuit and make a reaction-less transmission possible. For the connection to the other devices on the I^2C-bus (alignment forks), there are

two 6-point connectors (J1 and J2). The permanent I^2C slave address of the ADC is x6A. The analog signals that are to be digitized reach the ADC via two 10-point connectors J5 and J6 (on the right and left respectively in Figure 5.3). These also redirect +6 VDC for the power supply of the pressure sensors in the manifolds, where voltage stabilizers convert that to +5 VDC.

The 12 input channels of the ADC (numbered 0 - 11) are equipped with voltage dividers for adaptation to the impedance and the maximum range of the ADC which is given by the reference voltage of +4.5 V. All voltages higher than that are "cut off" and yield the maximum value. This range of $0 - 4.5$ V gives a resolution of 4.3988 mV/bit, corresponding to 0.1955 mbar/bit and 0.9775 mbar/bit for the 100- and 500-mbar sensor respectively. Signals from the 100-mbar sensors are read out by channels 0 and 1 for one manifold and 4 and 5 for the other. The readout by two channels each is done because of the availability of channels and to increase redundancy. The signals from the 500-mbar sensors are read out by channels 2 and 6, once for each sensor. Channels 3 and 7 receive the +5 VDC supply voltage of the sensors to be able to recognize erroneous behaviour due to power problems. Channel 8 measures the supply voltage of +5 VDC downstream with respect to the voltage stabilizer, channel 9 measures the supply voltage of +6 VDC upstream. Channel 10 is not occupied and channel 11 supplies the ADC with its reference voltage.

The voltage division mentioned earlier is caused by resistors in a low-pass filter (LPF). The ratio of the resistances depends on the range of the signals. For the sensors (channels 0,1,2,4,5 and 6) this range is $0.3\text{ V} - 4.3\text{ V}$, so the division factor can be close to 1. Values of 240 Ω and 100 kΩ with a tolerance of 1% were chosen, which ideally yields a factor of 0.9976 that has to be multiplied with the input voltage coming from the sensors. For the remaining channels 3,7,8 and 9, two resistors of 100 kΩ with a tolerance of 1% each are used, yielding a factor of 0.5.

The PADC boards were manufactured by two firms. The actual manufacturing was done by *Häusermann GmbH*[?] in Gars, Austria. The electrical components were added by *Kuttig Electronic GmbH*[?] in Roetgen, Germany. They are installed in an aluminum housing made by *Bopla Gehäuse Systeme GmbH*[?] in Bünde, Germany, that is painted in the "house color" of our institute (Figure 5.4).

5.4. Irradiation test

The PADC boards for the Muon Barrel system will be operating under intense radiation conditions. Therefore the boards as a whole and the microcontrollers have to prove that they can be operational as long as the experiment continues ($\geq$10 years). The tests for radiation hardness of the various PADC versions were done at two locations. The proton irradiation test was done at the The Svedberg Laboratory (TSL) in Uppsala, Sweden, the neutron irradiation test was done at Atomki in Debrecen, Hungary. During these tests the functions of the MiniCrate were emulated by the USB-I^2C-converter described earlier.

In the proton irradiation test the boards were exposed to a proton beam, coming

Figure 5.4.: The PADC board in its pink housing. The lid, carrying a label with information on the board, is not shown here.

from a cyclotron facility, with proton energies of 48 MeV, 95 MeV and 171 MeV. The result of this test was that the board with the AT90S8535 failed at about 30% of the aimed number of protons, while the other boards worked perfectly.

The neutron irradiation test was done with an average neutron energy of 3.5 MeV and a maximum of 20 MeV coming from a Be-target that was bombarded with 17 MeV protons. In this process photons are emitted as well with a typical gamma dose/neutron flux ratio of $3 - 5 \cdot 10^{-10}$ rad $\cdot$ cm^2 $\cdot$ s/neutron where the neutron flux was $1 \cdot 10^{11}$ n/cm^2. None of the boards showed any errors during this test.

5.5. Magnet test

Another aspect of the environment the PADC boards will operate in, is the magnetic field. Its strength in the muon barrel region will not be quite as high as inside the solenoid, but can still reach strengths of up to 2 Tesla. To study the effect of the magnetic field on the microcontrollers and the whole board, a test was performed (with help from Dr. H. Reithler and M. Sowa) with a magnet of the *II. Physikalisches Institut A* of the RWTH Aachen, that kindly allowed us to use their facility. The test included four PADC boards with the following microcontrollers: AT90S8535, ATmega8535, MAX127 and MAX1138. In addition a MAX127-chip was mounted on flexible cabling which allowed more freedom of movement in the magnetic field.

For this test a LabVIEW software was developed that combined the read-out routines for the various microcontrollers and that autmatically stored the data in a recognizable text file. The analog signals from the pressure sensors were simulated by arbitrary but fixed voltages generated by a power supply and some voltage dividers prepared by H. Szczesny.

Before and after the magnet test, a measurement of the analog voltages was carried

out at $B = 0$ T, which acts as a reference for the measurements in the magnetic field. Also before the magnet test, all input channels of the PADC's were checked for irregularities. The input voltages before and after the voltage dividers on the boards (Low Pass Filters) were measured with a digital multimeter. Another measurement of the voltages after the dividers was done while the channels were addressed to be read out via the I^2C-bus (active state). These measurements showed that the boards with the MAX127-chip had differences between the active and inactive state of the ADC-channels of up to 20 mV, because this chip was not designed for an input range of $0 - 5$ V, as already mentioned in section 5.3.2.

During the magnet test itself data were taken with the software mentioned above at $B = 1.5$ T, which is high enough for effects to become visible. To see if the magnetic field has an effect on the whole board, also other components than the ADC-chips were positioned between the magnet poles. For the Atmel versions these were the ATtiny26 and the optocouplers and for the MAXIm version this was the voltage stabilizer. To simulate the effect that the magnetic field is generally not perpendicular to the surface of the board, it was titled as much as the space between the poles alowed. The exact angle (roughly 20°) is unknown because this was simply done by hand, as can be seen in Figure 5.5. For a better study of this effect, the MAX127 mounted on the cables was used. Its surface could be positioned perpendicular as well as parallel to the magnetic field. The details can be found in Appendix A.

The read-out software experienced problems with the Atmel versions of the board. These are the same as described in section 5.3.1. The read-out could be accomplished by proper timing, but an attempt to reset the board caused a blockage that had to be solved manually for every run.

The diagrams in Appendix A show the voltages measured by channel 0 (arbitrary selection) of the various boards. The ADC-values do not change more than the allowed 1 bit, which shows that the functionality of the PADC boards is not compromised by the presence of the magnetic field.

At this time it was decided that the PADC board with the MAX1138 was going to be used for mass-production. It did not have large differences between active and inactive state like the MAX127, probably because this chip was already designed for an input range of $0 - 5$ V. The advantage over the Atmel chips, certainly the AT90S8535, was the direct communication via the I^2C-bus and the functionality without the need for time-consuming software development. It also has a higher resolution than the Atmel chips.

5.6. Temperature test

All components on the PADC board should be able to work in a range of temperatures according to their data sheets. Although the range during the experiment will not be very wide, since it is located 100 m below the surface where the temperature is very constant, the conditions during test periods in a laboratory on the surface might vary. To see whether an increase in temperature, which is most likely to happen, has any effect on

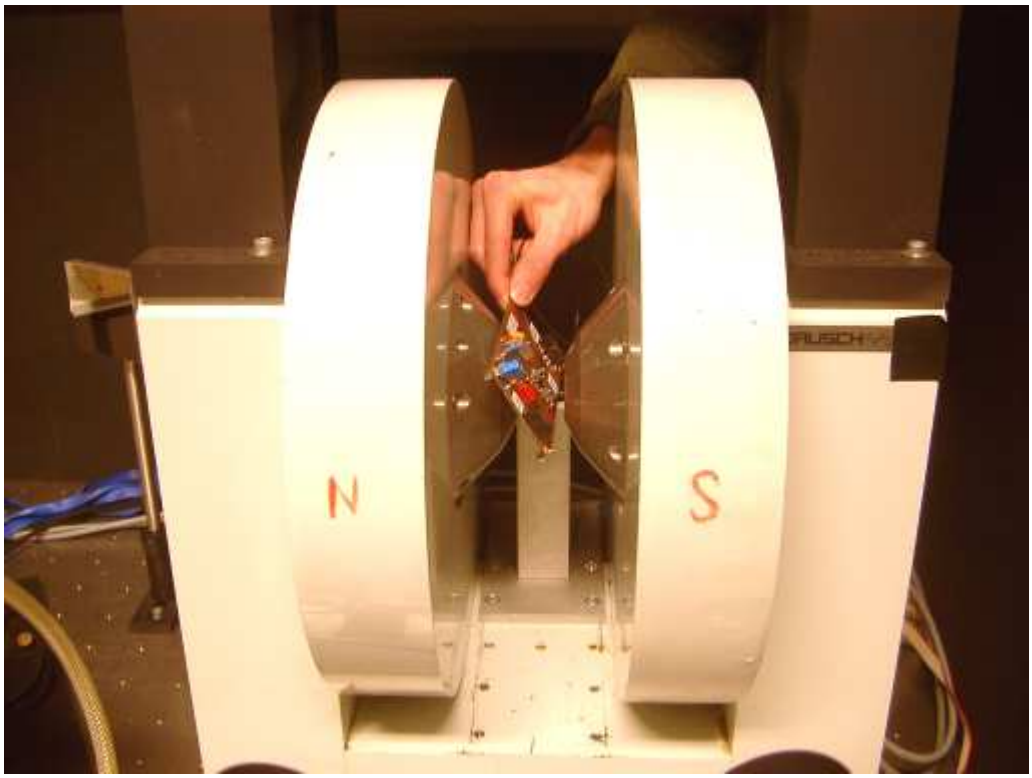

Figure 5.5.: During the magnet test the boards were held between the magnet poles at various positions. To simulate the effect of a non-perpendicular magnetic field, the boards were tilted from time to time as much as the space between the poles allowed.

the PADC board, it was put in an oven. Normally this "Haereus" oven is used to warm up the glue that is used in the construction of the muon chambers.

For this test one board (Ser.No. 284, calibrated and chosen at random) was equipped with plastic "feet" to avoid short-circuits and placed inside the oven. The oven heater was set to the lowest value, but still this would be too warm for this purpose. To compensate the heating, the door was left open a little, while the temperature inside the oven was monitored with a small thermometer.

Again some communication problems with the board occurred and delayed the test. With the help of H. Szczesny, this was found to be a malfunction of the RS232-I^2C-converter, which was then fixed and the test was continued. At room temperature ($t = 25\ ^\circ C$) a normal PADC calibration run (chapter 6) was performed. Then the calibration was repeated at a temperature of about $t = 45\ ^\circ C$. This way the first run could be used as reference to cancel the effect of the longer cables. To compare the two runs, the ADC-values of the first run were subtracted from the values of the second run. This difference is shown in Figure 5.6 for all points of channel 0. Differences of ± 4.4 mV (± 1 bit) are allowed and as one can see, the values stay within this range. The differences for the other channels show the same behaviour. This leads to the conclusion that the PADC

board can operate correctly in relatively high temperatures.

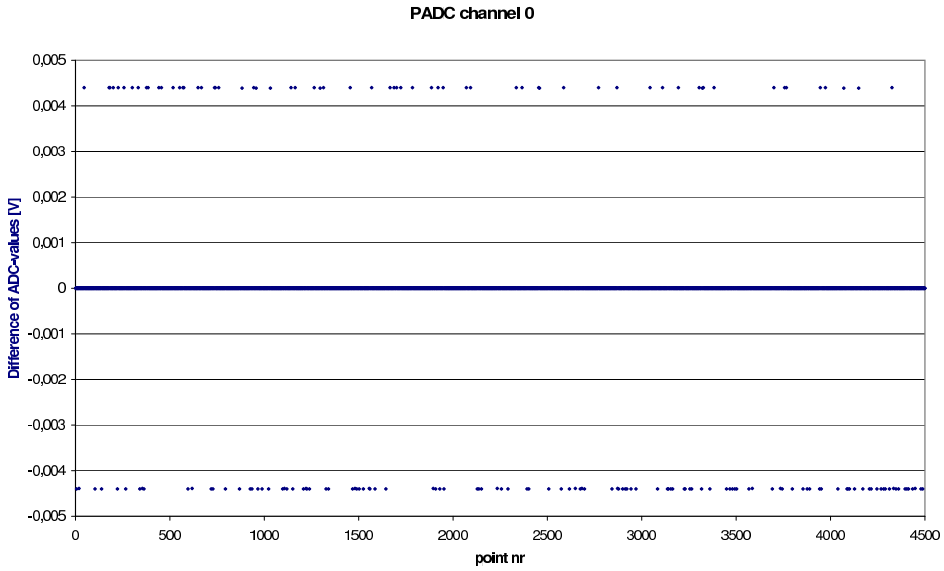

Figure 5.6.: The difference of the ADC-values measured in two calibation runs at different temperatures is shown for all points of such a run (chapter 6). The y-axis shows the value (voltage) of the second run ($t = 45\ ^\circ\mathrm{C}$) minus that of the first run ($t = 25\ ^\circ\mathrm{C}$). The differences are not beyond the allowed range of $\pm 4.4\,\mathrm{mV}$ or ± 1 bit.

6. PADC test and calibration

6.1. Motivation

All detector components have to undergo quality control tests to guarantee their functionality. This means that also the PADC boards need to be tested after their assembly. After a first simple test in the electronics workshop of the institute, the boards are calibrated. This calibration is in fact a linearity check of the PADC channels that is regarded as quality control as well, since all components of the PADC board are used over a longer period of time. Only channels 0-7 are actually calibrated since channels 8 and 9 only measure the voltage up- and downstream the voltage stabilizer. For these two channels quality control implies the constance of their measurements during the calibration run. If the values are not constant (a difference with respect to the first measurement of 1 bit or 4.4 mV is allowed) this indicates either a problem with that particular channel or a problem with the power supply of the PADC board. In both cases this has to be investigated.

6.2. Functionality test

The first test is a general functionality test. In the electronics workshop, every PADC board is connected to a power supply and to two pressure manifold prototypes that measure the pressure in the room. They are read out a few times via the I^2C-bus with the help of the RS232-I^2C-translator described in 5.2 and a computer with LabVIEW-software. This software sends the appropriate commands for the read-out and writes data it receives to a text file in hexadecimal form. It is essentially the same as the software used in the magnet test.

The read out values for each channel are compared to values in a reference table. The measured values may vary per board, because of pressure variations and small variations of the board's components. If the differences with respect to the reference values are not larger than a few digits, the PADC board is considered to be functioning and ready for the calibration.

6.3. Calibration

For the calibration of the PADC boards, a part of the facility is used, that is used in the calibration of the pressure sensors. A schematic setup is shown in Figure 6.1.

Using the 16-bit DAC[1] of two *NI6014*-boards, made by *National Instruments*, a computer can generate analog voltages. Via two "Link Boxes" and a connector board (*Anschlusskarte AK*) these analog voltages are measured by the PADC board and by the NI6014-boards. The PADC board and the RS232-I^{2}C-translator are connected to a power supply, supplying +6 VDC and +5 VDC respectively. An important factor in the measurements is the voltage division caused by resistors not only on the PADC board, as described in 5.3.3, but also in the Link Boxes and on the connector board. The principle of voltage division is shown in Figure 6.2, where the current I through both resistors is the same, but the voltage ($U = \sum_i U_i$) is divided according to the resistances, as follows from Ohm's law $U_i = R_i \cdot I$.

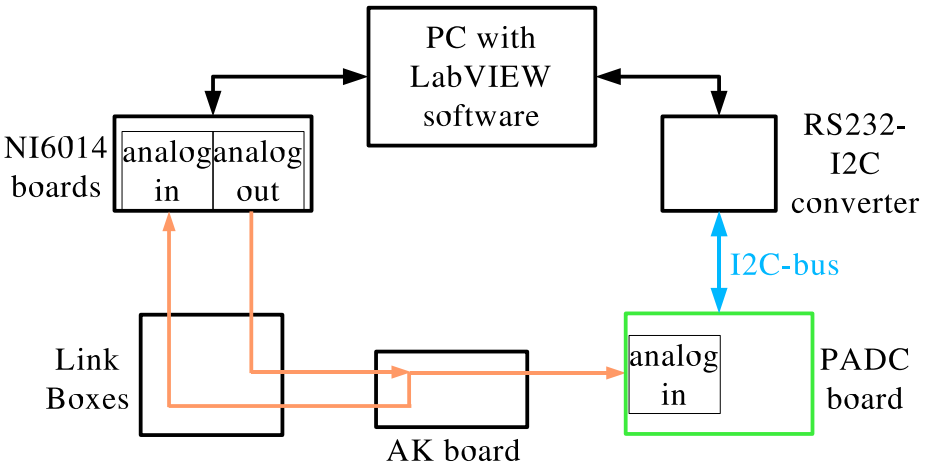

Figure 6.1.: Schematic setup of the PADC calibration. The analog output voltages at the NI6014 boards are controlled by software. The voltages are then distributed (AK board) to the analog input of the PADC board and the NI6014 boards. The same software handles the read-out of both ADC's and the storage of data.

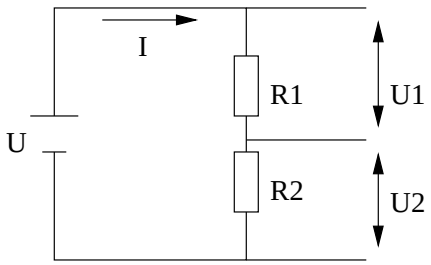

Figure 6.2.: The voltage U is divided according to the resistances: $U1 = R1 \cdot I$ and $U2 = R2 \cdot I$. This occurs in the Link Boxes for the input channels of the NI6014 board and on the PADC board for its input channels.

[1] **D**igital to **A**nalog **C**onverter

NI6014 boards

These both have a 16-bit DAC with two output channels and a 16-bit ADC with 16 input channels. In the PADC calibration analog voltages are generated on all four output channels. Also four input channels (two per board) are used for digitizing the analog voltages parallel to the PADC. Since the PADC uses a 10-bit ADC, the NI6014-channels have a much higher resolution and can be used to monitor the calibration process. They could detect much smaller variations in the analog voltages than the PADC and therefore are suitable as a reference in case a PADC channel shows any anomalies.

Link Boxes

Two Link Boxes are attached to the calibration rack that is used in the sensor-calibration. Each has eight 10-pin connectors for the 16 input channels and one 14-pin connector for the two output channels of a NI6014 board. Low Pass Filters (LPF) were added to the input channels by the electronics workshop. To make a comparison between PADC values and NI6014 values easier, the same voltage dividers are used on the PADC board. The division factors generated by these resistors were precisely measured.

Connector board AK

This board distributes the analog output voltages, which are generated at the 4 'Analog Out'-channels of the Link Boxes, to the inputs of the PADC board as well as to 4 input channels of the NI6014 board. This results in a digitization of every output voltage by two independent ADC's. The matching is as described in table 6.1. The presence of voltage dividers on the AK changes the expected division factors for channels 6 and 7 of the NI6014 board. The combination of resistances in the voltage dividers of the Link Boxes and the AK yields a division factor of 3.0048 for these channels, where this would be 1.0024 without the AK.

$U_{in}1$ (AO, LB 1, Ch 0) connected to NI6014 Ch 6 and PADC Ch 7
$U_{in}2$ (AO, LB 1, Ch 1) connected to NI6014 Ch 7 and PADC Ch 3
$U_{in}3$ (AO, LB 2, Ch 0) connected to NI6014 Ch 4 and PADC Ch 0,1,4,5
$U_{in}4$ (AO, LB 2, Ch 1) connected to NI6014 Ch 5 and PADC Ch 2,6

Table 6.1.: Matching of analog output channels (AO) to the input channels of the PADC and the NI6014 board.

6.4. Software

The software for the calibration was completely developed in LabVIEW and was a combination of a few smaller pieces of software.

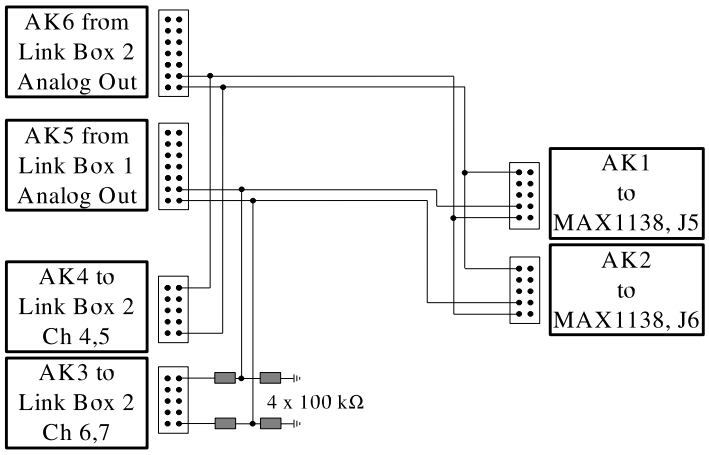

Figure 6.3.: Block diagram of the connector board AK.

The first piece is the read-out part that was already used before, e.g. during the magnet test (5.5). This sends the commands necessary for the communication with the PADC board via the RS232-bus of the computer. The digitized (hexadecimal) data are converted to decimal numbers ("digits") and then to voltages using the formula $U_{PADC}[V] = digit \cdot \frac{4.5\,\mathrm{V}}{1023}$. The hexadecimal data and the corresponding voltages are written to an ASCII[2]-textfile.

Also a small piece of software was created, that sets the voltage on the analog output channels of the NI6014 boards. It does this before every read-out cycle of the 10 channels of the PADC. Starting at 0 V and incrementing by 1 mV per cycle, it takes 4501 loops to reach the final 4.5 V which is the maximum voltage the PADC can handle. The increments of 1 mV are smaller than the PADC-resolution, which causes the digitized output to remain constant for ca. 4 consecutive loops.

The combination of these two pieces of software was then integrated into the existing software for the calibration of pressure sensors. This makes it possible to use the same software for all calibrations. An even bigger advantage was the possibility to select input channels of the NI6014 boards that had to be read out, which was already available in the existing software. In every loop the NI6014 channels are read out 1000 times while the PADC channels are read out only once due to the limited speed of the I^2C-bus and the translator board. Each data point for a NI6014 channel is the average of these 1000 measurements. These data then only had to be written to the same file as the PADC-data. The filename and path are generated automatically with the start of a calibration run. The manual for the PADC calibration with a short description of the software can be found in Appendix B.

[2] **A**merican **S**tandard **C**ode for **I**nformation **I**nterchange

6.5. Evaluation and results

The evaluation of the calibration data is done offline with MS[3] Excel. After the ASCII-file is loaded into a spreadsheet, the difference between the analog voltage at the output of the NI6014 board (nominal voltage U_{nom}) and the measured voltage U_{meas} (after digitization) is calculated for every data point for every PADC and NI6014 channel (except PADC channels 8 and 9). The nominal voltage is assumed to be absolutely reliable.

The resulting distribution (Figure ?? in Appendix B) can be fitted by a linear approximation $y = ax + b$, where $y = U_{nom} - U_{meas}$ and x is the point number (this corresponds to U_{nom} in [mV]). The parameters a and b are the gradient and offset of the distribution. These are used to correct the measured voltages and fit them to the nominal voltages. In the first step the gradient is eliminated, giving the diagram of Figure ?? in Appendix B for the difference between nominal and scaled voltages U_{scal}. Figure ?? in Appendix B shows the difference between nominal and corrected voltages U_{corr}, where also the offset is eliminated. The corrected ("true") voltages can thus be obtained by multiplying the mesaured voltages U_{meas} with a "scaling factor" A, which is connected to parameter a via

$$A = \frac{1}{1-a} \quad , \tag{6.1}$$

and then subtracting the offset (parameter b).

The typical structure of the (final) distribution (blue points in Figure 6.4) is a result of the increment per loop in the calibration (1 mV) being smaller than the PADC resolution (4.4 mV). The pink points represent the so-called "smoothness" S of the measured data. This is defined as

$$S\,[mV] = \frac{Y_1 + Y_3}{2} - Y_2, \tag{6.2}$$

where Y_1, Y_2 and Y_3 are three consecutive (measured) data points. The output of the PADC increases in discrete steps with increasing nominal voltage. Again because of the small increments, these steps will be 0 or 1 digit ideally, corresponding to 0 or 4.4 mV. S will therefore be 0 or ± 2.2 mV. A PADC board is considered good, if the difference between nominal voltage U_{nom} and corrected measured data U_{corr} is not over a certain limit for 5 or more points ($<$1.1 ‰). This limit is based on the experience gathered during tests and depends on the channel. As described in section 5.3.3, channels 3 and 7 of the PADC are equipped with a LPF that divides the voltage in half (scaling factor: $\frac{1}{1/2} = 2$), whereas for channels 0,1,2,4,5 and 6 the scaling factor is $1/0.9976 = 1.0024$. The limit for the latter channels is a difference of ± 3 mV, which gives a total width of a little more than 1 bit (4.4 mV). For channels 3 and 7 this limit is doubled, because in the correction of measured values where these are multiplied with the scaling factor of 2, the differences are multiplied with the same factor. For the channels of the NI6014 board the limits are 0.6 mV. This is much smaller than for the PADC channels because

[3] Microsoft Corporation

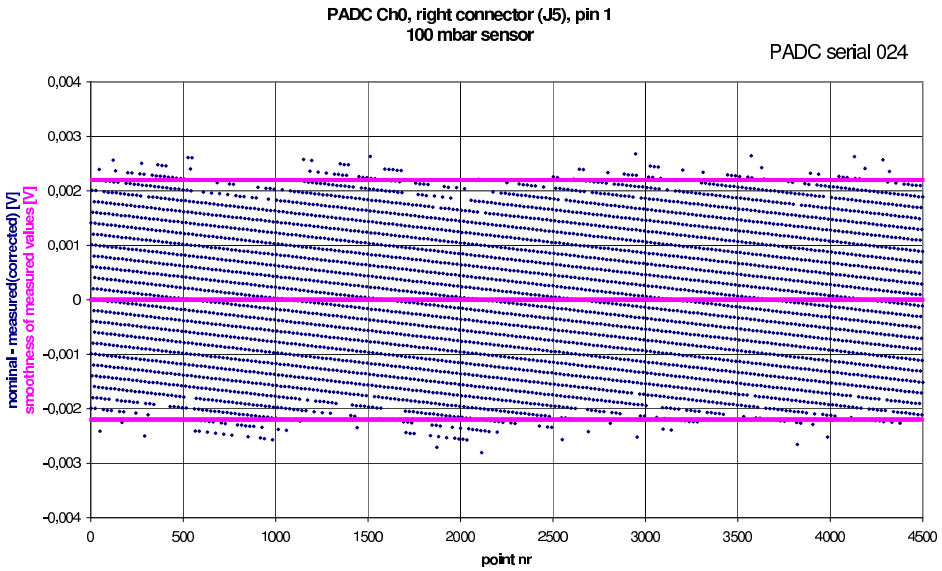

Figure 6.4.: A complete I^2C data transfer with the transitions between High and Low of the SDA and SCL line, the numbers representing the number of bits needed.

of the difference in resolution, although part of this is canceled out by the scaling factor of $1/0.3328 = 3.005$ which has the same effect as with the PADC channels 3 and 7.

For channels 8 and 9 only an offset is determined. This is the difference between expected and measured voltage. The expected voltages are 2.5 V for channel 8, resulting from 5 V coming from the voltage stabilizer divided by 2, and 3 V for channel 9, resulting from 6 V coming from the power supply divided by 2. Especially for channel 8 it is important that the voltage is constant to ensure that the boards' components can function correctly. For both channels differences of 1 digit or 4.4 mV with respect to the first value are allowed.

The calibration of the PADC is in fact the measurement of the ratio of the resistors on the PADC board and a linearity check of its channels as part of quality control.

The results of the calibration and the following evaluation can be found in a calibration report. This Excel spreadsheet contains the original data, a tab with calculations and a "Header" tab with the set of calibration parameters for each channel that will be used for the experiment. Besides the parameters, the Header tab contains additional information, like the standard deviation of the distributions before and after correction, and the number of points exceeding the limit. Below this table of parameters are tables with the descriptions of the PADC channels and which analog output channels they are connected to. The file also contains separate diagrams like Figure 6.4 for each channel. To be independent from the operating system, a pdf-version of the report is generated, containing the Header and the diagrams, and a printed version is kept in the laboratory

where the calibration takes place. The most important regions of the Header (see Appendix B), namely that with the calibration parameters and quality control are given a background color (green and yellow respectively).

Overall conclusion:	GOOD			Nominal - Measured [V]		# points	
Channel	Scaling factor	Offset [V]		Max.after scaling	Limit	above limit	Conclusion
$nominal minus PADC Ch0	1,000650365	-0,001411974		0,002804093	0,003	0	GOOD
$nominal minus PADC Ch1	1,00062819	-0,001332748		0,002855633	0,003	0	GOOD
$nominal minus PADC Ch2	1,00057773	-0,000875992		0,002783849	0,003	0	GOOD
$nominal minus PADC Ch3	1,995886517	-0,001509335		0,005432899	0,006	0	GOOD
$nominal minus PADC Ch4	1,0006504	-0,001386631		0,002836282	0,003	0	GOOD
$nominal minus PADC Ch5	1,000616909	-0,001358219		0,002998772	0,003	0	GOOD
$nominal minus PADC Ch6	1,000588821	-0,000905823		0,002953406	0,003	0	GOOD
$nominal minus PADC Ch7	1,995806789	-0,001992849		0,00551344	0,006	0	GOOD
$PADC Ch8 *	-	-0,013634288		2,51613	0,0044	0	GOOD
$PADC Ch9 *	-	-0,0176		3,0176	0,0044	0	GOOD

Figure 6.5.: Example of a part of the Header (see Appendix B) from a calibration report. In the top left corner the overall conclusion "Good" or "Bad" of quality control. The details for each channel are found on the right in the yellow region. Directly below the overall conclusion is the set of Scaling factors and Offsets for each PADC channel in the green region.

That the calibration parameters are reproducible can be seen from table 6.2. This shows the absolute and relative differences of the scaling factors and offsets. Δ indicates the difference between two measurements ("OLD" is a calibration run from 20. January 2005, "NEW" is a run from 17. March 2005): $\Delta x = x_{NEW} - x_{OLD}$. The relative difference is $\Delta\%x\ [\%] = 100\% \cdot \frac{\Delta x}{x_{OLD}}$. The relative differences of the scaling factors are all smaller than $0.1\%_0$, which shows that the ratio of resistances is constant. The offsets have relative differences of up to 7% (for channel 1), which looks like a lot, but corresponds to $\Delta\text{Offset} \approx 0.1$ mV. This is well below the resolution of the PADC and will have a negligible effect on the measurements in the experiment.

The result of the temperature test in section ?? can also be seen as proof that the parameters are reproducible, even at different temperatures.

6.6. Status of the calibration

The current status of the PADC calibrations is that for all 250 boards the functionality test as well as the calibration run has been performed. During the functionality test only one board was rejected while 5 others could be repaired. From the boards that passed the first test, 5 experienced problems during the calibration. For 2 of these boards the problem occurred in a PADC channel. This was caused by someone who accidentally adjusted the voltage of the power supply measured by PADC channel 9. Therefore this channel showed larger differences than allowed, as described above (6.1). PADC channel 8 showed no problems, which explains why all other channels functioned properly. A second calibration run for these boards eliminated the problem. For the other 3 boards some or all of the NI6014 channels were reported as "bad" after evaluation, while all of the PADC

	Δ Scaling factor	Δ% Scaling factor [%]	Δ Offset [V]	Δ% Offset [%]
PADC Ch0	$1.5222 \cdot 10^{-5}$	0.001521211	$-9.2933 \cdot 10^{-5}$	6.581778418
PADC Ch1	$2.1811 \cdot 10^{-5}$	0.002179731	-0.000092099	6.910458691
PADC Ch2	$2.653 \cdot 10^{-5}$	0.002651468	-0.000031321	3.575489274
PADC Ch3	$2.7662 \cdot 10^{-5}$	0.001385951	-0.000015595	1.033236492
PADC Ch4	$-1.7394 \cdot 10^{-5}$	-0.001738269	$-2.902 \cdot 10^{-6}$	0.209284229
PADC Ch5	$1.1074 \cdot 10^{-5}$	0.001106717	$-8.5535 \cdot 10^{-5}$	6.297585294
PADC Ch6	$2.875 \cdot 10^{-6}$	0.000287331	$-2.555 \cdot 10^{-6}$	0.282063935
PADC Ch7	$-1.8133 \cdot 10^{-5}$	-0.000908555	$-2.0524 \cdot 10^{-5}$	1.029882344
PADC Ch8	-	-	-0.000573828	4.208712622
PADC Ch9	-	-	0	0

Table 6.2.: Differences (Δ) and relative differences (Δ%x) of calibration parameters obtained from two calibration runs for one PADC board. They show that these parameters are reproducible.

channels were "good". Looking at the data and plots, the effects that were measured by the NI6014 channels were too small for the PADC channels to be noticed. Since checking the connector board had no result, there might have been interference with other software on the computer that influenced either the input or the analog output channels of the NI6014 board(s). A second calibration run for the concerned PADC boards showed no problems. Also the evaluation of the boards that were calibrated immediately afterwards did not show any sign of this. This indicates that the NI6014 board had a temporary problem which occurred very rarely and is no reason for concern.

Up to now the evaluation of ca. 25 PADC boards is yet to be done, while the others were all labeled "OK". Ca. 50 boards are still in Aachen, the others were already shipped to CERN, where they are attached to the muon chambers in their pink housing.

7. Practice

7.1. Test with sensors and PADC

As a final test for measuring the pressure in the muon chambers during the CMS experiment a test was performed in Aachen that included both pressure manifolds and a PADC board. All used parts had already been calibrated before the test. The look-up tables for the sensors as well as the table with PADC parameters had been made.

A normal calibration run for 10 manifolds was carried out, but with two of them (Ser.No. 529 and 530) customized cables were used that allowed for a simultaneous read-out by the NI6014 board (Channels 00 to 03 on Link Box 2), as usual, and the PADC board (Ser.No. 215). The schematic setup is shown in Figure 7.1. In this test the combined software for PADC and sensor calibration read out the PADC data and the voltages from the sensors and the Baratron devices. The goal of this test was to reproduce the pressures exerted on the sensors and then to compare the results with the pressures measured by the Baratron devices. To be able to compare the sets of data, all voltage divisions that took place had to be considered and corrected. For the PADC board this was taken care of with the parameters from the calibration. For the NI6014 board, which also handles the data from the Baratron devices, this was done with the scaling factors calculated from the known resistor values. MS Excel was used to combine data, calibration parameters and look-up tables.

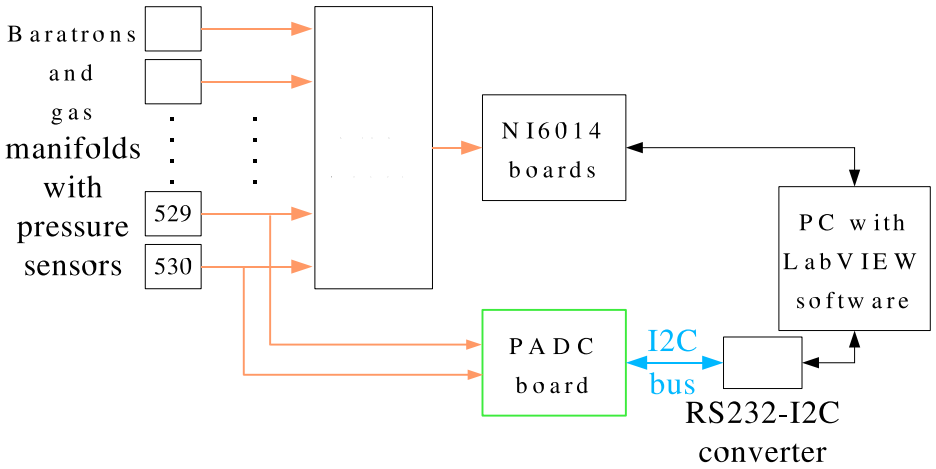

Figure 7.1.: Gesamttest.

For the PADC data the first step was to convert the hexadecimal data back to the voltages as they would have been without divisions ("true voltages") using the calibration parameters. These voltages were then converted to pressures using the look-up tables and interpolation. For the NI6014 channels connected to the sensors, the procedure was similar, only that the original data were already voltages. For the Baratron devices, apart from the correction for the voltage division at the Link Box, a correction for an offset with respect to the relative pressure was needed, because the devices measure different values for the atmospheric pressure. This "zero-point offset" is not constant, but shows a small shift when comparing reference measurements of the atmospheric pressure before and after the sensor calibrations. For this evaluation two values for this offset were tried: one "assumed" value, based on longtime experience from the calibrations and one average value, calculated from the reference measurements before and after this calibration run (10 measurements each). The "zero-point shift" effect is currently under investigation by using two additional Baratron devices as a reference. A similar behaviour is seen for the pressure sensors, where the output voltage at atmospheric pressure before and after the calibration differs by a few mV.

Comparing the data was done by subtracting the pressures from the various devices from one-another and plotting the result as a function of the point number. To try and include all voltage division effects, the channels of the NI6014 were also calibrated in the way as this is normally done for the PADC boards. The scaling factors for these channels were at first calculated from the known resistor values, but the lists did not include the offsets for these channels. The calibration provided the full set of parameters, which was then used in the calculations.

The result for the difference between the differential pressure measured by the Baratron devices and channel 0 of the PADC board (Δp) is shown in Figure 7.2. The mean value and the standard deviation for all channels is shown in Figure 7.3. The ideal scenario would result in a narrow distribution around $\Delta p = 0$. It is widened because of the limited resolution of the ADC that is used and the granularity of the look-up tables. The observed mean values of Δp are less than ± 1 mbar when comparing the reconstructed pressures measured by the NI6014 and PADC channels. Comparing the pressures measured by the NI6014 or PADC channels and the Baratron data, the mean value of Δp is generally larger than that. This could indicate that the value that was used for the Baratrons' zero-point shift is not correct. A correct value will have to be obtained from the measurements mentioned above. They could also help understand the sensors' zero-point shift, which could also be partly responsible for the offset in the diagram. The difference between NI6014 and PADC channels would then be so small, because they both receive the output voltages of the sensors, which cancels the effect.

7.2. Test beam 2004

A chance to test the whole read-out system would have been given by the Test beam during two weeks in October and November of 2004 at CERN. The goal of this Test beam was to reconstruct muon tracks with data from two muon chambers, a MB1 chamber,

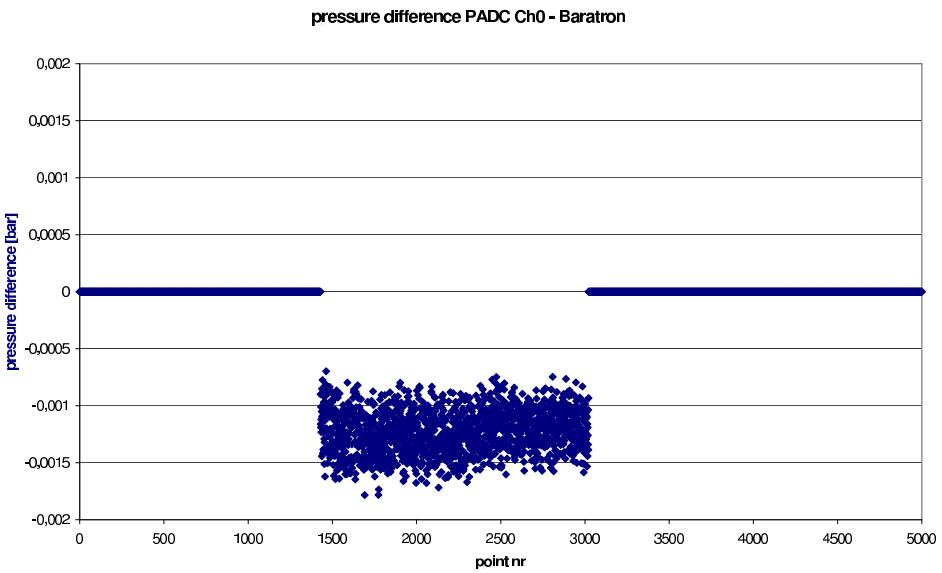

Figure 7.2.: Gesamttest

built in Aachen, and a MB2 chamber equipped with a MB3 MiniCrate. A team from Aachen helped setting up for the test and also took shifts for data-taking.

Figure 7.4 shows the setup of the two muon chambers in the test area, a relatively small space in the huge hall of the north area at the CERN Prévessin site. The smaller chamber on the right is the MB1, the other the "MB3". The chambers could be moved laterally to one another and one of them could be rotated up to 60° to simulate bent muon tracks. The pink boxes of the PADC boards and one gas manifold on each chamber are clearly visible. The other gas manifolds are situated on the opposite side of each chamber together with the MiniCrates. The forks of the alignment system are situated along the other two sides of the chambers and are not visible here, but indicated by the green arrows. The muon beam is indicated by the blue dashed arrow.

Unfortunately, from the pressure-side-of-view, there had been a change of the connector for the I^2C-bus on the MiniCrate. The corresponding connector of the cable that connects the various devices to the MiniCrate had not been changed yet. The small red 6-pin connectors that are used for the I^2C-bus on the PADC board as well as on the forks of the alignment system were replaced on the MiniCrate by a larger 10-pin connector that only uses 6 of those pins. Also the length of the cable would have to be adjusted, because it was much too short as it was. These replacements and adjustments were under way, but had not yet been applied to the two muon chambers that were used..

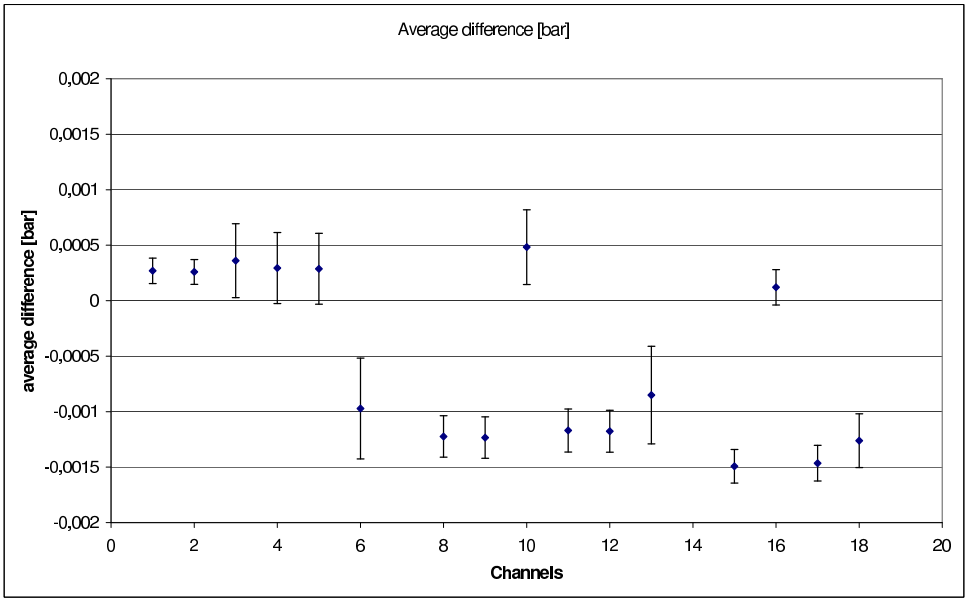

Figure 7.3.: Gesamttest

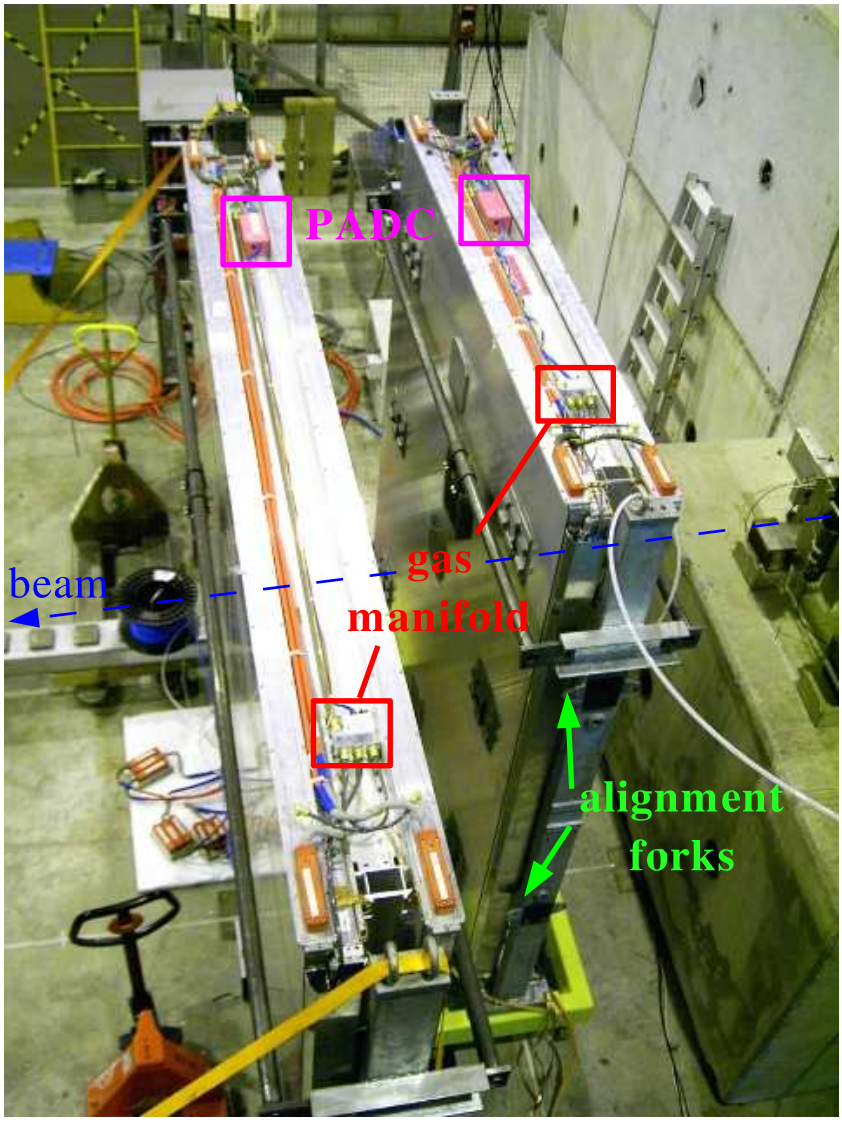

Figure 7.4.: The pink boxes of the PADC boards and one gas manifold on each chamber are clearly visible. The forks of the alignment system are situated along the sides of the chambers and are not visible here, but indicated by the green arrows.

A. Results of the magnet test

Shown below are the results of the magnet test that was carried out with all diferent versions of the PADC board. As described in 5.5, the boards were held between the magnet poles at a few different positions per board to test their sensitivity with respect to the magnetic field. The different positions are indicated by the numbers directly above, and the vertical lines in the plots. The details can be found in the caption of every plot with the strength of the magnetic field, the region of the PADC board that was held between the poles and "tilt" when the board was tilted. For all ADC's changes of the output values by ± 1 bit are allowed.

The plots for the Atmel boards show very constant values. This can be explained by the 8-bit resolution, the smallest of all PADC versions (1 digit corresponds to ca. 19 mV). Even if there were fluctuations of up to a few mV, the ADC would not notice them.

The channels of the MAX127 are much more unsteady. These have a 12-bit resolution, which is the highest of the tested boards (1 digit corresponds to ca. 1 mV). Together with the missing impedance adaptation (described in 5.5) this can explain the switching between two values. The plot for board nr. 12 shows a distinct spike at point nr. 41. This is were positions were switched and probably contact was made with a magnet pole.

The explanation for the spike in Figure A.5 is probably the same. It occurs shortly after a change of position, when the board could easily have slipped away. After the spike the output value is constant. Like this channel, the other input channels of this chip give no indication that the chip's functionality is compromised.

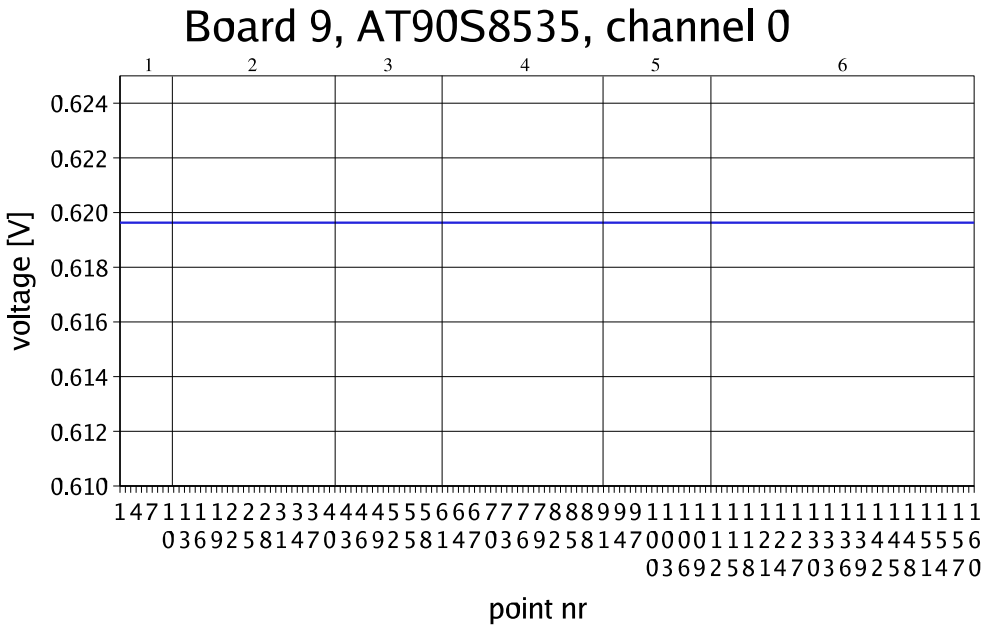

Figure A.1.: 1: $B = 0$ T, 2: $B = 1.5$ T microcontroller, 3: $B = 1.5$ T microcontroller tilt, 4: $B = 1.5$ T ATtiny26, 5: $B = 1.5$ T ATtiny26 tilt, 6: $B = 0$ T.

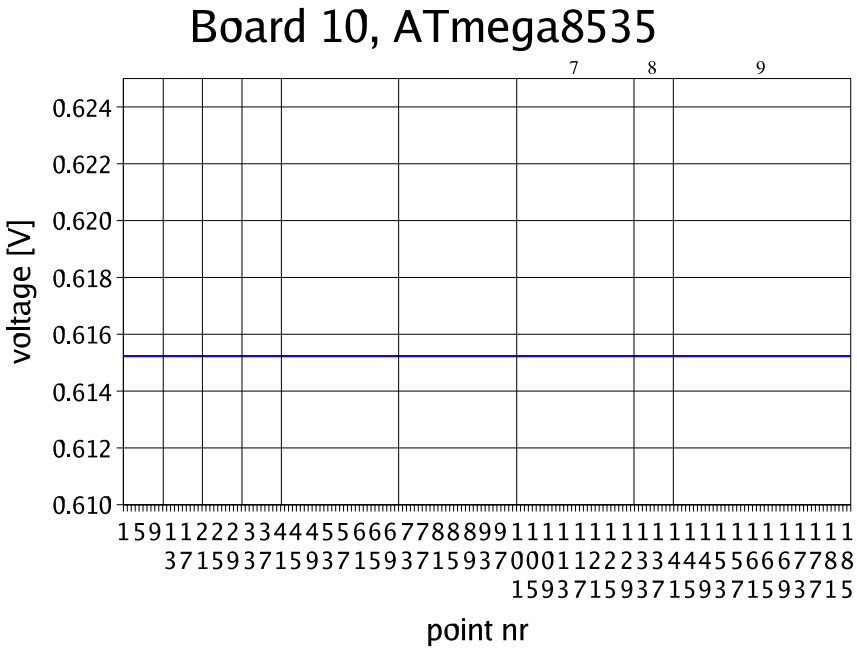

Figure A.2.: 1: $B = 0$ T, 2: $B = 1.5$ T optocoupler, 3: $B = 1.5$ T microcontroller, 4: $B = 1.5$ T ATtiny26, 5: $B = 1.5$ T optocoupler, 6: $B = 1.5$ T microcontroller, 7: $B = 1.5$ T ATtiny26, 8: $B = 1.5$ T microcontroller tilt, 9: $B = 0$ T.

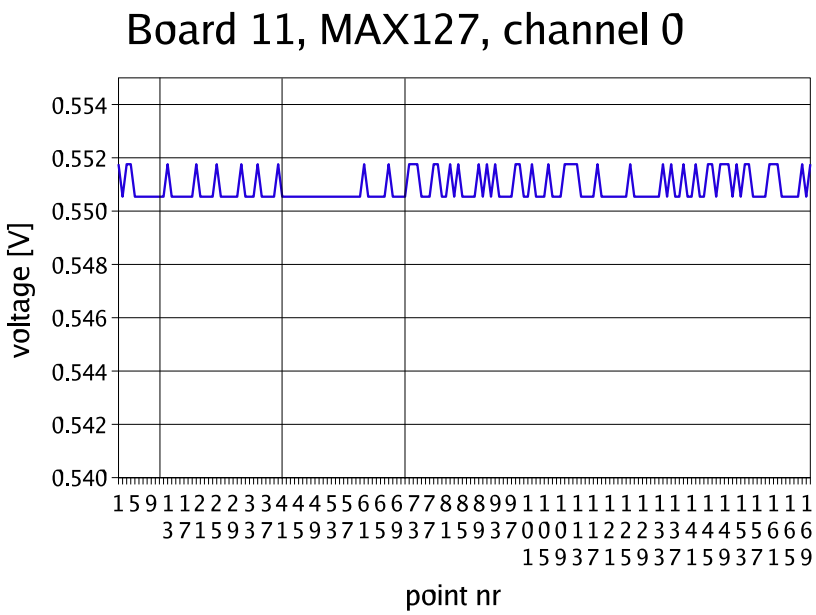

Figure A.3.: 1: $B = 0$ T, 2: $B = 1.5$ T parallel to plane of chip, 3: $B = 1.5$ T perpendicular to plane of chip, 4: $B = 0$ T. For this ADC 1 bit corresponds to 1.2 mV.

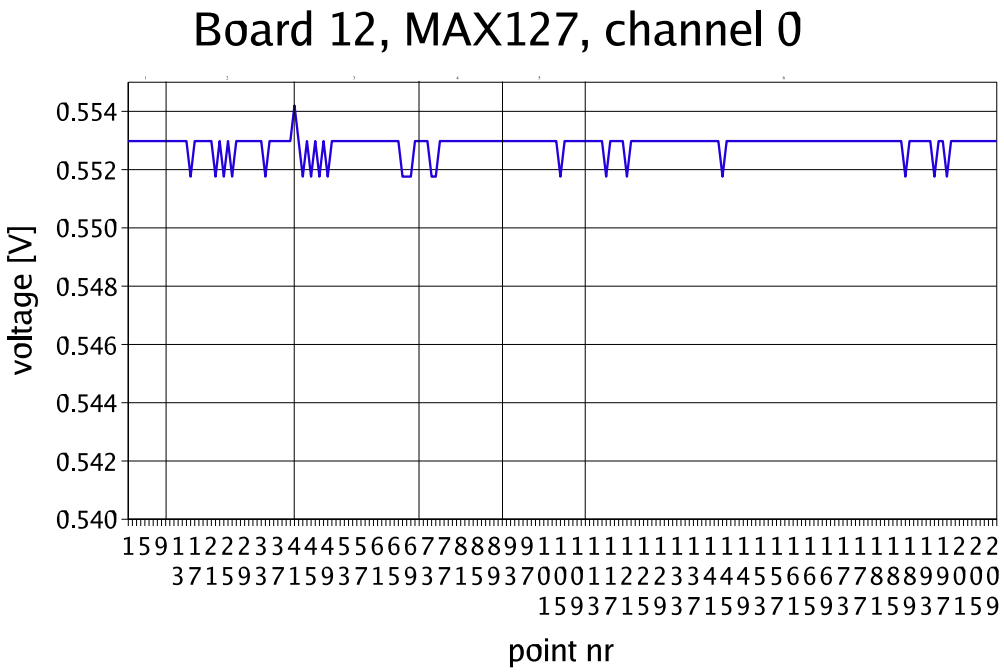

Figure A.4.: 1: $B = 0$ T, 2: $B = 1.5$ T microcontroller, 3: $B = 1.5$ T microcontroller tilt, 4: $B = 1.5$ T voltage stabilizer, 5: $B = 1.5$ T voltage stabilizer tilt, 6: $B = 0$ T. For this ADC 1 bit corresponds to 1.2 mV.

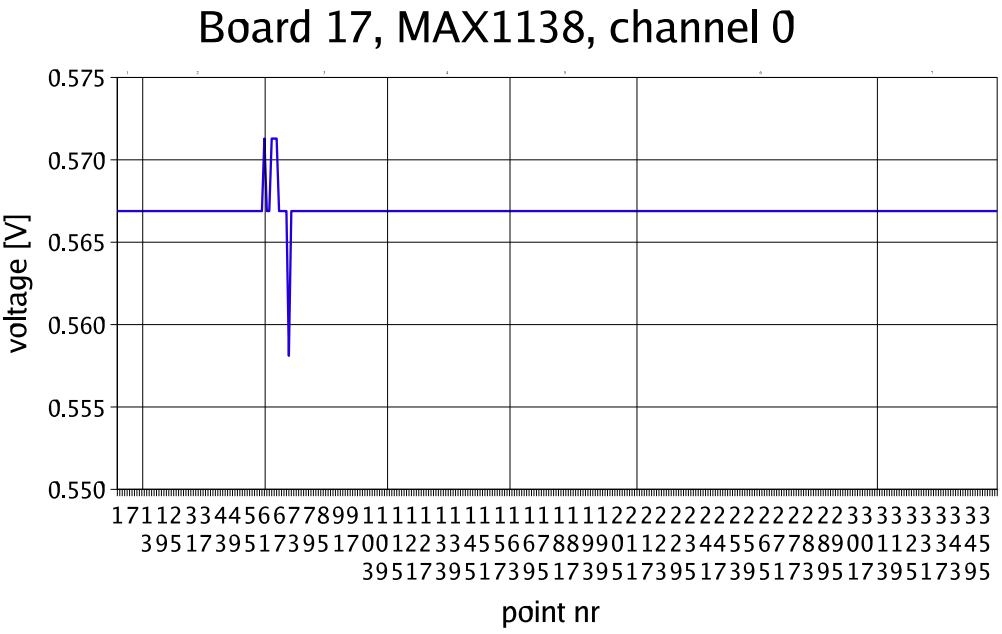

Figure A.5.: 1: $B = 0$ T, 2: $B = 1.5$ T microcontroller, 3: $B = 1.5$ T microcontroller tilt, 4: $B = 1.5$ T optocoupler, 5: $B = 1.5$ T optocoupler tilt, 6: $B = 1.5$ T voltage stabilizer, 7: $B = 0$ T. For this ADC 1 bit corresponds to 4.4 mV.

B. Process of calibration

The PADC boards were all calibrated with the LabVIEW program "PADC_kalibrationV1.0.vi". The manual for this program is found below with a screenshot of (part of) the front panel, as it is seen by a user. Also shown is a part of the ASCII-file the data are stored in.

Calibration of PADC boards – manual

by P. Rütten, Aachen 27.08.04

Hardware

- Place the PADC board that is to be calibrated in the pink PADC box and connect the cables for powersupply, I^2C-bus (both comming from the RS232-I^2C connector board "PADC–TB–A") and two signal cables (comming from connector board "AK"). Please watch the labels on the boards and on the cables.
- The power supply for the RS232-I^2C connector board and the PADC boad should be set to 5 V and 6 V respectively.
- Connect the remaining four plugs on the AK to the corresponding plugs (again watch the labels) on the Link Boxes.

Software

- Start the LabView Programm "PADC_kalibrationV1.0.vi". If there is no shortcut on the desktop, this can be found in the folder "D:\PADC\Currently used".
- In the left part of the working space, at "Analog Out voltages at Link Boxes", one can set the voltage at the analog outputs ("Analog Out") of the two Link Boxes (two channels respectively) to be constant or increasing from zero until the value

set. The increase in voltage will occur in a number of equidistant steps which can be set in the blue area of the working space at "Loops to do". In a typical calibration all four channels are set to 4,500 V and "Increasing" and the number of "Loops to do" is set to 4501.

- Then, in the left part at "PADC Board No.", it should be indicated which PADC board is being calibrated by entering the three-digit serial number, which can be found in the upper right corner of the PADC board.
- In the blue part at "Link Box 1/2" one can indicate which devices are read out by the National Instruments NI6014 board by activating the green buttons.
- Also in the blue part one can set the waiting time between the read-out cycles at "Waiting time before/after closing EV". While calibrating a PADC board, these should be set to zero, so the time span for a calibration is minimized.
- At the bottom of the blue part, under "Run by", the name of the person who does the calibration. Also there is the possibility to insert comments (under "Comment").

When everything is set correctly, the program can be started by leftclicking the arrow button in the top left corner of the window.
The actual calibration of the PADC board is started when the button "run PADC calibration" in the blue part is pressed.

Written down in the logbook are:

- date and initials
- the (three-digit) serial number of the PADC board
- the filename of the measurement, which can be found in the window under "filename"
- comments.

Shown below are the plots that result from the different stages of the calculations. The difference between nominal and measured data yields a distribution with a gradient and an offset. The calibration parameters are extracted from the gradient and offset in two steps. First the measured data are corrected for the gradient (Figure B.2) and then for the offset (Figure B.3). This procedure is repeated for every channel (except channels 8 and 9). The plots in the calibration report also include the so-called smoothness of the measured data for each channel.

The calibration parameters of all channels are joined together in a table in the Header of the calibartion report (Figure B.4).

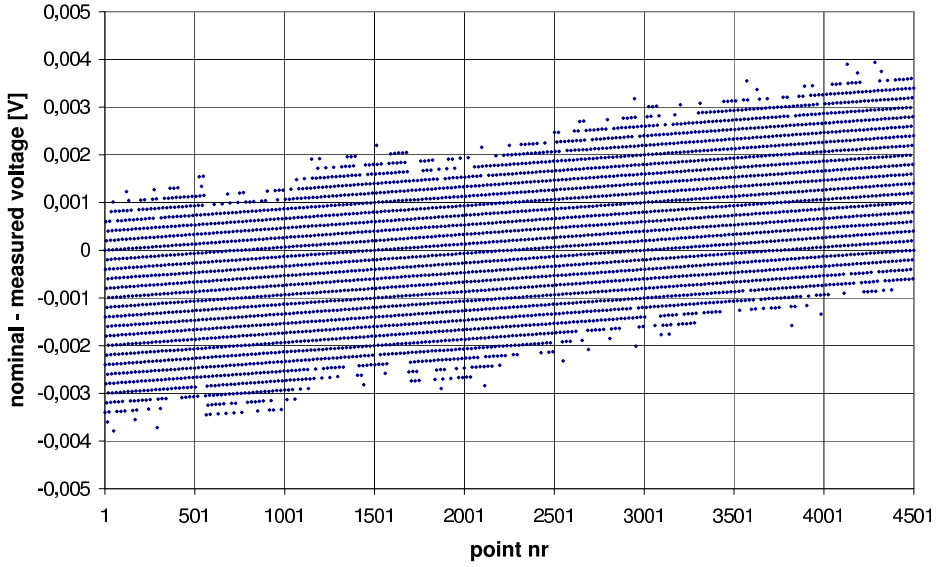

Figure B.1.: The difference between nominal and measured voltage plotted against the point number results in a distribution with a gradient and an offset.

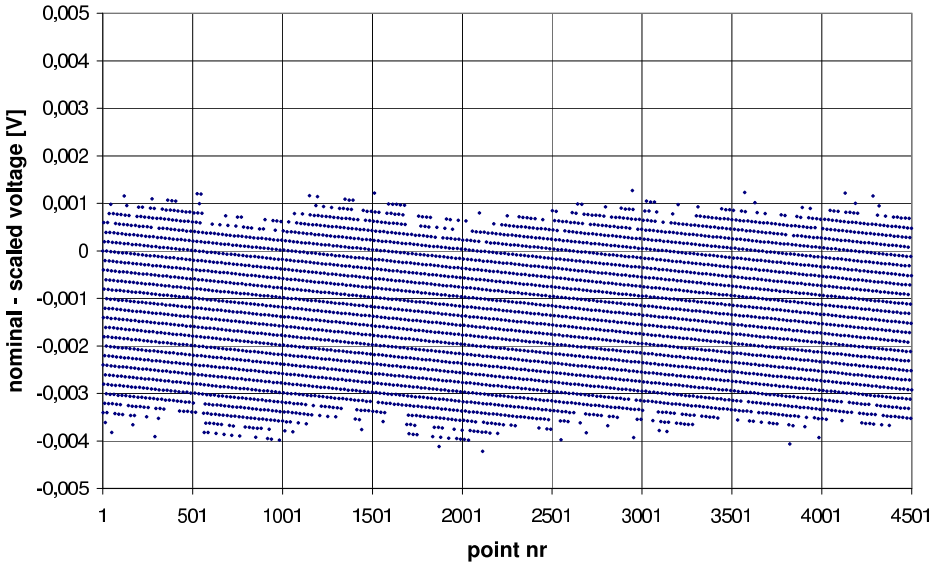

Figure B.2.: In the second step, the scaling factor is used to eliminate the gradient and produce this plot. The distribution now only has an offset left.

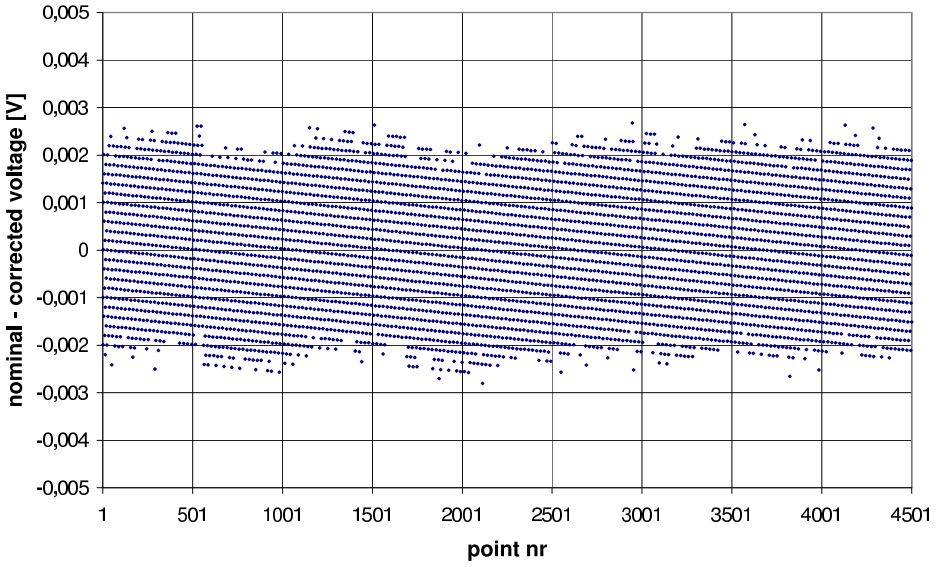

Figure B.3.: After the measured data have also been corrected for the offset, the final result is a distribution around zero. The typical structure is a result of the increment per loop in the calibration (1 mV) being smaller than the PADC resolution (4.4 mV)

Overall conclusion:	GOOD		Standard deviation σ [V]		Nominal - Measured [V]		# points	
Channel	Scaling factor	Offset [V]	before scaling	after scaling	Max.after scaling	Limit	above limit	Conclusion
nominal minus PADC Ch0	1.000566	-0.000808	0.001498	0.001306	0.003111	0.003	2	GOOD
nominal minus PADC Ch1	1.000534	-0.000717	0.001475	0.001303	0.002852	0.003	0	GOOD
nominal minus PADC Ch2	1.000514	-0.000207	0.001468	0.001308	0.002979	0.003	0	GOOD
nominal minus PADC Ch3	1.992700	-0.000753	0.647285	0.002573	0.005587	0.006	0	GOOD
nominal minus PADC Ch4	1.000559	-0.000776	0.001492	0.001304	0.003109	0.003	2	GOOD
nominal minus PADC Ch5	1.000532	-0.000735	0.001474	0.001303	0.002977	0.003	0	GOOD
nominal minus PADC Ch6	1.000516	-0.000212	0.001464	0.001303	0.002847	0.003	0	GOOD
nominal minus PADC Ch7	1.991926	-0.001312	0.647031	0.002571	0.005361	0.006	0	GOOD
PADC Ch8 *	-	-0.029330	-	-	2.529330	0.004	0	GOOD
PADC Ch9 *	-	-0.021990	-	-	3.021990	0.004	0	GOOD
nominal minus NI6014 Ch4	1.002514	-0.001475	0.003261	0.000130	0.000512	0.001	0	GOOD
nominal minus NI6014 Ch5	1.002637	-0.000982	0.003420	0.000136	0.000524	0.001	0	GOOD
nominal minus NI6014 Ch6	3.005274	-0.002263	0.866978	0.000148	0.000506	0.001	0	GOOD
nominal minus NI6014 Ch7	3.017494	-0.047642	0.868729	0.000140	0.000492	0.001	0	GOOD
			theoretical	data				
PADC Ch0 minus NI6014 Ch4			0.001313	0.001300	0.002900	0.003	0	GOOD
PADC Ch1 minus NI6014 Ch4			0.001309	0.001299	0.002756	0.003	0	GOOD
PADC Ch2 minus NI6014 Ch5			0.001315	0.001301	0.002862	0.003	0	GOOD
PADC Ch3 minus NI6014 Ch7			0.002577	0.002573	0.005574	0.006	0	GOOD
PADC Ch4 minus NI6014 Ch4			0.001310	0.001298	0.002960	0.003	0	GOOD
PADC Ch5 minus NI6014 Ch4			0.001309	0.001298	0.002955	0.003	0	GOOD
PADC Ch6 minus NI6014 Ch5			0.001310	0.001296	0.002751	0.003	0	GOOD
PADC Ch7 minus NI6014 Ch6			0.002575	0.002571	0.005353	0.006	0	GOOD

Figure B.4.: Part of the Header from a calibration report with the calibration parameters. In the top left corner the overall conclusion "Good" or "Bad" of quality control. The details for each channel are found on the right in the yellow region. Directly below the overall conclusion is the set of Scaling factors and Offsets for each PADC channel in the green region.

B. Process of calibration

List of Figures

List of Tables